Graduate Theses, Dissertations, and Problem Reports

2022

Functionally Magnetic Gradient Copper-Nickel Material Fabricated via Directed Energy Deposition

Vy Tran Phuong Nguyen
West Virginia University, vtn0001@mix.wvu.edu

Follow this and additional works at: https://researchrepository.wvu.edu/etd

Part of the Industrial Engineering Commons, and the Metallurgy Commons

Functionally Magnetic Gradient Copper-Nickel Material Fabricated via Directed Energy Deposition

Vy Nguyen

**Thesis submitted to the
College of Engineering & Mineral Resources
at West Virginia University**

**in partial fulfillment of the requirements
for the degree of**

**Master of Science
in
Industrial Engineering**

Zhichao Liu, Ph.D., Chair
Thorsten Wuest, Ph.D.
Xueyan Song, Ph.D.

Department of Industrial and Management Systems Engineering

Morgantown, West Virginia
January 2022

ABSTRACT

Functionally Magnetic Gradient Copper-Nickel Material Fabricated via Directed Energy Deposition

Vy Nguyen

Functionally gradient materials (FGMs) of CuSn10 and Inconel 718 were fabricated via a hybrid directed energy deposition (DED) system. The objective of the present thesis is to determine the feasibility of manufacturing CuSn10 and Inconel 718 FGMs via DED and investigate the physical and mechanical properties and the microstructures of the resulting FGMs. The physical tests comprised of conductivity and Seebeck coefficient measurements. The microstructure analysis and mechanical testing include microscopic imaging, scanning electron microscopy (SEM), energy dispersive spectroscopy (EDS), and hardness test. In addition, compressive strength test was performed to analyze the interface bonding behaviors.

Table of Contents

List of Figures

List of Tables

1. Introduction

1.1. Directed Energy Deposition Method for Additive Manufacturing

1.1.1. Introduction, Principles, and Applications

Directed Energy Deposition (DED), one of the seven additive manufacturing (AM) families, is defined as "an AM process in which focused thermal energy is used to fuse materials by melting as they are being deposited" (Gibson et al., 2014). DED was developed in 1997 at John Hopkins University by Frank Arcellak, who later commercialized the innovation through his own company Aeromet (Molitch-Hou, 2018).

The heat source commonly utilized in DED processes are lasers, though electron beams and plasma are being studied and experimented in lab settings as potential alternatives. DED can work with a wide range of materials, including metals, polymers, ceramics, and composites, in either powder (45-150 micron) or wire (1-3 mm) form. Nonetheless, despite the variety of compatible materials, DED is more commonly applied in metal AM. The powder materials are supplied using a nozzle feeding method (Figure 1a) while wire materials are supplied through a wire spool (Figure 1b).
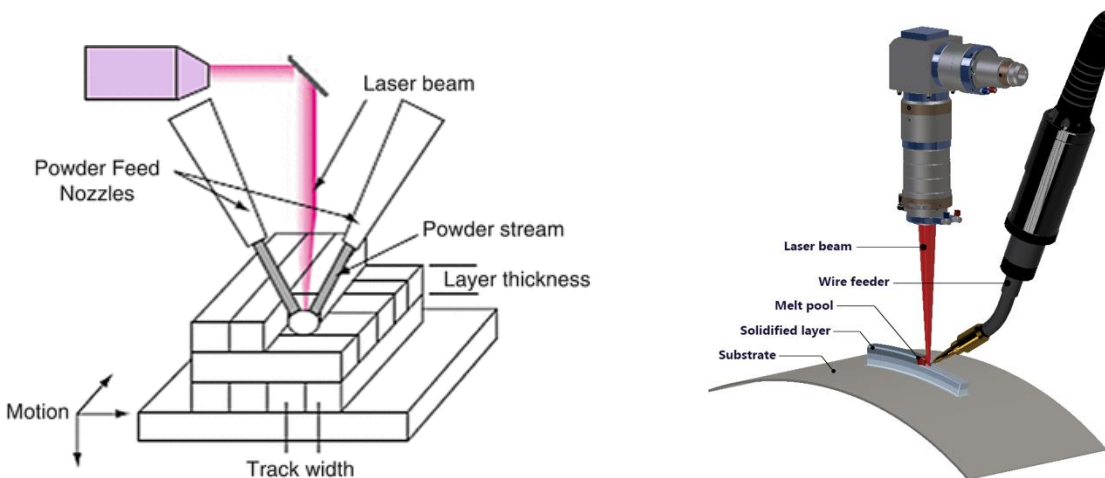
Figure 1. Example schematics of DED systems; Powder-based (left) and Wire-based (right)
(Gibson et al., 2014)

During DED processes, it is crucial to ensure the key parameters are closely controlled as they directly affect the part quality. The key parameters consist of laser power, layer thickness, powder feeding rate, and scanning speed. Theoretically, support structures can be added during DED processes if it is acceptable to stop and restart the process for every material changeover. However, it is apparent that this practice is costly in both time and labor, which explains why it is often stated that support structure cannot be added to DED-printed parts. Instead, a higher dimensional build platform (five dimensions or higher) is often utilized when overhang structures are involved in DED processes.

Additionally, DED is often referred to as Laser Engineered Net Shaping (LENS) due to its ability to produce near net-shaped parts. Thanks to the ability to apply materials directly into the heat pool, when coupled with the use of a multi-dimensional platform, DED allows the deposition of new features onto existing structures, as well as the ability to produce curvy surfaces. For that reason, DED is a well-known technique to repair damaged parts in many industries, especially aerospace (Molitch-Hou, 2018). DED applications consist of developing or fabricating new products, repairing, or enhancing existing structures, and tooling or coating on quick-wearing parts.

1.1.2. The Pros and Cons of DED

DED is known for many advantages. As aforementioned, DED allows the manufacturing of near net-shaped parts, requiring minimal to no post-processing nor additional tooling, as well as the notable ability to repair or enhance parts thanks to the direct deposition of materials. According to ASTM International, DED is capable of producing larger-sized parts thanks to its superior build volume of 1000 sq.mm and up, claiming advantages of the cost of production, as well as the build and post-processing time.

Furthermore, DED does not only work with a wide variety of materials, but it also permits the manufacturing of non-homogenous parts consisting of multiple materials, which is crucial to the present thesis. DED also provides unmatchable control on microstructure and material properties. Additionally, it is imperative to acknowledge that DED can be coupled with subtractive manufacturing (i.e., CNC machining) methods to create a hybrid system. Such hybrid systems are beneficial in improving part quality post AM.

On the contrary, DED also proposes many challenges. While the build volume and large part size may bring DED advantages when compared to other metal AM processes, it is noted that larger DED printers often only produce simpler parts with low resolution. The larger DED parts, the more vulnerable they are to residual stress. The surface finish on parts produced using DED are rough and often require post-machining to improve the quality. In addition, DED are subjected to porosity as well as cavities and cracks on some materials. Last but not least, residual stress, surface tension, and uneven powder distribution may also be problematic in DED (Gibson et al., 2014).

1.2. Functionally Gradient Materials (FGMs): Introduction, Classifications, and Applications

Functionally Gradient or Graded Materials (FGMs) were often referred to as "innovative materials in which final properties varies gradually with dimensions" (Singh et al., 2017). In other words, FGMs comprise of varying compositions and thus, varying material and mechanical properties. The different properties in different segments of the specimen allow FGMs to outperform single-material parts in criterium including but not limited to strength, toughness, thermal conductivity, wear and tear, corrosion, and oxidization resistance (Carroll et al., 2016; Zhang & Liou, 2019). The focus of this thesis remains limited to metallic FGMs or the FGMs of two or more metals and/or their alloys (Yan et al., 2019).

FGMs can be classified by size, into thin and thick (or bulk) FGMs. Thin FGMs refer to the multi-material coating on existing surfaces or structures, while thick FGMs are complete 3D structure with gradient of materials (K. Makarenko & Shishkovsky, 2020; Singh et al., 2017). In addition to size classification, FGMs can also be classified using the types of gradients, including stepwise and continuous gradient (Chen & Liou, 2018; Singh et al., 2017; Yan et al., 2019). Stepwise gradient describes an abrupt transition from one single-material region to another, while continuous gradient involves compositional or intermediate layers in-between the single-material phases. Furthermore, FGMs can also be classified based on the fabrication methods (K. Makarenko et al., 2020). Lastly, they can be classified into varying chemical composition FGMs or varying spatial structure (e.g., lattice, porosity) FGMs (Chen & Liou, 2018).

The concept of FGMs were first introduced in 1980s as materials with high-temperature resistance for thermal barriers (Koizumi, 1997). Since then, FGMs have been thoroughly studied and its application exceedingly evolved. In recent times, FGMs applications can be found in many demanding industries such as aerospace, marine, nuclear, electronics, biomedical, and energy conversion (Carroll et al., 2016; K. Makarenko et al., 2020; Meng et al., 2020; Singh et al., 2017).

1.3. The manufacturing of FGMs

K. Makarenko et al. (2020) discussed the three main groups of FGMs fabricating techniques: deposition-based (vapor deposition, electrodeposition, thermal spray method), liquid-state (centrifugal force methods, slip casting, tape casting, infiltration method, and Langmuir–Blodgett method), and solid-state methods (powder metallurgy, friction stir welding, and additive manufacturing). Singh et al. (2017) acknowledged three conventional methods to manufacture FGMs: vapor deposition, powder metallurgy, and centrifugal casting.

Due to the longer length of the process and its high energy consumption, vapor deposition is limited to thin FGMs fabrication. The method is ruled uneconomical due to the high cost and building time for manufacturing bulk FGMs. Despite being the better methods to produce FGMs out of the three, both powder metallurgy and centrifugal casting pose trivial challenges. Power metallurgy can only produce stepwise FGMs while centrifugal casting can only fabricate cylindrical parts. The same findings were also reported by Yan et al. (2019). Furthermore, the joining of two dissimilar materials often leads to defects due to the mismatched atomic structures and material properties. When using conventional methods, intermediate layers or specific conditions must be applied to prevent such defects (Carroll et al., 2016).

On the other hand, fabricating FGMs through additive manufacturing (AM) approaches was discussed to be cost-effective, waste minimal, and allowable for complicated shapes without the extra step of assembly (K. Makarenko et al., 2020). According to the American Society for Testing and Materials standard, AM is defined as "a process of joining materials to make objects from 3D model data, usually layer upon layer." From the first process recognition in the late 1980s, AM has grown rapidly to extend the boundaries of manufacturing. With the layer-upon-layer building principle, AM simplifies in-situ controls, permitting a smoother fabrication of joint-material parts such as FGMs. It is also reported that AM processes generally require less time and effort, especially in the tooling and post-processing stages, and produce less waste (Yan et al., 2019). Singh et al. (2017) wrote that AM are preferred due to the freedom to design and fabricate complicated designs with a higher utilization of materials and a lower energy insensitivity.

Yan et al. (2019) mentioned two commonly used AM techniques to produce FGMs: selective laser melting (SLM), which belongs to the powder bed fusion family, and directed energy deposition (DED), which is included in the laser metal deposition (LMD) processes. The two processes are powder-based with the complete melting of particles and are often utilized to fabricate metal parts. SLM process refers to "a powder bed fusion process used to produce objects from powdered materials using one or more lasers to selectively melt the particles at the surface, layer by layer, in an enclosed chamber." After each layer print, a new layer of powder is deposited on top of the print bed in preparation for the next. Meanwhile, DED process is defined as "an additive manufacturing process in which focused thermal energy is used to fuse materials by melting as they are being deposited" (Gibson et al., 2014). The powder materials are supplied through nozzles directly into the melt pool in DED process, as opposed to the use of a powder bed.
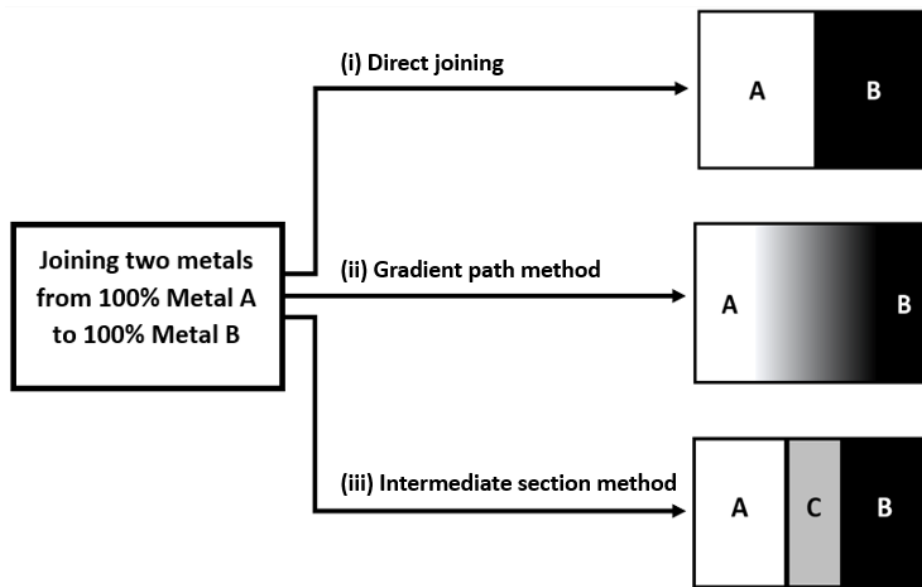
Figure 2. LMD Building Strategies for FGMs discussed by Yan et al., 2019

Thus, while SLM approach is argued to have a better geometric accuracy when compared to DED, it is more challenging to control the composition variation during print due to the use of the power bed. For that reason, SLM are often applied to produce varying lattice structure rather than varying composition FGMs. In DED systems, different types of powders can be stored in multiple hoppers and supplied during print, allowing a precise control over material composition (Carroll et al., 2016; Yan et al., 2019). K. Makarenko et al. (2020) determined DED to be superior in comparison to other AM techniques when it comes to FGMs fabrication, citing its low substrate deformation and high process automation. DED powder feeding rates can also be altered during print, making it a better choice for varying chemical composition FGMs. When compared to traditional wielding methods, Yao et al. (2021) indicated that DED processes have lower heat affected zone and better metallurgy bonds. Consequently, DED are often applied to produce FGMs for aerospace and automotive industrial demand, thanks to the ability to combine high-performing properties of two metals (Chen & Liou, 2018).

1.4. Copper-Nickel Alloy and its Application

Copper is a non-magnetic metal with high thermal and electrical conductivity. The soft metal is known for its high resistance against salt and alkaline corrosion (Karnati et al., 2015; Zhang et al., 2021). In contrast, nickel possess high strength, high toughness and performs well in extreme temperatures. Thus, the metal and its alloys are often utilized in aviation and space applications. Hence, when combining copper and nickel (including alloys) in manufacturing FGMs, the resulting product is expected to have the added high thermal and electrical conductivity, as well as high strength and toughness and the ability withstand high temperature conditions.

Copper-nickel FGMs were desirable in advance and technologically demanding industries such as space and aviation (K. Makarenko & Shishkovsky, 2020) and marine (Nickel Institute). Additionally, a wide range of applications for copper-nickel alloys were presented in Table 1.

Conventionally, there are two prominent grades of copper-nickel alloy utilized in marine applications: 90%Cu-10%Ni, and 70%Cu-30%Ni. Depends on the application of the finished alloys, different methods to manufacturing them were applied in order to maximize the quality and usability of the parts. As earlier discussed in Section 1.3. of the present thesis, the general challenges and limitations of manufacturing FGMs also applied to Cu-Ni-based FGMs, including higher costs and numerous restrictions on the gradient type and shape of specimens (Singh et al., 2017 and Yan et al., 2019). In contrast, AM techniques were discussed by Yao et al. (2021) to have a smaller heat affected zone and better metallurgy bonding between the regions. Hence, AM appeared to be the superior approach when it comes to the manufacturing of FGMs.

Table 1. Cu-Ni alloys & their applications (Nickel Institute)

Alloy	Applications	Alloy	Applications
90%Cu-10%Ni, and 70%Cu-30%Ni	Seawater cooling and firewater systems, heat exchangers, condensers and piping, platform riser and leg sheathing, boat hulls, oil coolers, hydraulic tubing, antimicrobial touch surfaces.	Cu-30%Ni-Cr	Forgings, cast seawater pumps and valve components.
Cu-Ni-Al	Shafts and bearing bushes, bolting, pump and valve trim, gears, fasteners.	Cu-Ni-Sn	Bearings and drill components, subsea connectors, valve actuator stems, lifting nuts, ROV lock-on devices, seawater pump components.

2. Literature Review

2.1. Related Works

The reviewed literatures for the present thesis can be categorized into four main groups: (1) literatures on FGMs of copper and other metals (including alloys), (2) literatures on FGMs of nickel and other metals (including alloys), and (3) literatures on FGMs of copper and nickel (including alloys) and (4) literatures on metals FGMs excluding copper, nickel, and their alloys.

2.1.1. Literatures on FGMs of copper and other metals (including alloys)

Dubinin et al. (2021) demonstrated the AM of soft magnetic FGMs between stainless steel (SS) 316L and Cu-12Al-2Fe via DED using the in-situ powder flow control method. K. Makarenko & Shishkovsky (2020) studied the structure of copper-iron via the manufacturing of stainless steel (SS) 316L and aluminum bronze FGMs. Two specimens were fabricated and studied. The first specimen included a single layer of bronze wedged in the middle of 50 layers of SS316. The second specimen were an alternating layered FGM of SS316 and bronze. Further analysis and an additional study (K. Makarenko et al., 2020) were conducted on the specimens.

Mikler et al., (2017) presented three case studies on magnetic FGMs. One of the case studies focused on the FGM of Fe-Si-B-Cu-Nb via preblended powder-based DED. It was mentioned that even though the feedstock was preblended, the alloys from all three case studies displayed relatively uniform microstructure and comparable magnetic properties in comparison to conventional manufacturing approaches.

Articek et al., (2013) studied the FGM of Cu and H13 tool steel in an attempt to introduce high thermal conductivity materials into steel utilized to serve the tool and die industry. The microstructure analysis showed sufficient metallurgical bonding between the regions. It was additionally discussed that the mechanical properties displayed by the LENS sample outperformed its casted counterpart, providing groundwork for further research for FGMs to be used in real life tool-and-die applications.

2.1.2. Literatures on FGMs of nickel and other metals (including alloys)

Chaudhary et al. (2020) successfully manufactured magnetic FGMs of nickel-iron and cobalt-iron via DED using the in-situ powder flow control method. Using the same method, (Ji et al., 2020) experimented the FGMs of Inconel 718 and Ti-6Al-4V with vanadium carbine intermediate layers to address the mismatched properties between the two chosen materials. In this study, the authors controlled the powder flows during prints by adjusting the material supplying plates' rotating velocity and the argon carrier gas flow.

Yarrapareddy et al., (2006) studied the nickel-tungsten carbine FGMs manufactured via laser-based direct metal deposition with preblended powder for industrial slurry erosion preventions. Shishkovsky et al. (2016) fabricated a structure consists of Ni-Cr-Al via laser cladding of Diamalloy 1005, a nickel-chromium alloy, and aluminum. Two of the three aforementioned case studies by Mikler et al., (2017) presented first, the magnetic FGMs of Fe-30 at.%Ni, and second, the magnetic permalloys of Ni-Fe-V and Ni-Fe-Mo. Yao et al. (2021) examined the effect of initial

temperature on DED-formed FGMs of Inconel 718 and Stellite-6 at two different setting: room temperature and 300ºC.

One prominent FGMs material thoroughly studied and experimented with nickel components is SS. Kim et al. (2021) studied the defect-free FGMs between Inconel 718 and SS316L via DED. The fabricated FGM consisted of 11 levels, with 12 layers per level, ranging from pure Inconel 718 to pure SS316L with 10% weight (% wt.) ratio increment. It was concluded that DED aids the otherwise difficult to achieve via conventional wielding methods bonding between Inconel 718 and SS316L. Ghanavati et al. (2021) fabricated three specimens of FGMs from the same materials using the same technique: a straight joint FGM of 100% SS316L on 100% Inconel 718; a gradient FGM with three levels: 100% SS316L, 50% SS316L/ 50% Inconel 718, and 100% Inconel 718; and lastly, an incremental 20% wt. from 100% SS316L to 100% Inconel 718.

Yang et al., (2022) investigated the defects caused by stepwise FGM of 100% SS316 and 100% Inconel 718 in comparisons to FGM with compositional gradient of 10% and 25%wt. The straight-joint of the two materials resulted in cracks at the interface of the two materials while no mentions of such defects other than vertical cracks within regions were found in the continuously graded samples.

Besides Inconel 718, Inconel 625 is also a popular choice for nickel based FGMs. Zhang & Liou (2019) fabricated an FGM of SS136L and Inconel 625 via DED comprised of three levels: pure SS316, a preblended combination of 50% wt SS316L and 50% wt Inconel 625, and pure Inconel 625. Carroll et al. (2016) studied SS306L and Inconel 625 FGM manufactured via in-situ gradient DED. It was concluded that the fabricated FGM did not possess any sharp compositional, structural, nor microstructural boundaries. Meng et al. (2020) utilized DED with laser synchronous preheating to produce FGMs of Inconel 625 and SS 316L with 10% compositional interval from 100% Inconel 625 to 100% SS 316L.

2.1.3. Literatures on FGMs of copper and nickel (including alloys)

Karnati et al. (2015) fabricated FGMs of pure copper and pure nickel via DED using preblended powders. The gradient included 4 levels, ranging from 100% Ni to 25% Ni/ 75% Cu, with 25% wt increment for each level. The authors stated 100% Cu was omitted from the design due to limitations of the printing system. Yadav et al. (2020) conducted a similar study on pure copper-nickel FGM. The authors studied effects of the parameter and manufactured a 5-zone FGM including: 100% Ni, 25% Cu/ 75% Ni, 50% Cu/ 50% Ni, 75% Cu/ 25% Ni, and 100% Cu from preblended powders using DED.

In contrast, Lin et al. (2006) conducted a study on in-situ flow-rate control DED method to fabricate copper-nickel FGMs. The authors examined two systems: a dual powder DED and a wire-powder DED. The wire-powder system achieved a uniformly gradient structure, while the dual powder system failed due to the presence of unmelt powder. It was explained that the different melting point of copper and nickel was the reason behind the defect. A wire-powder system where the material with the higher melting temperature is in its wire form was further recommended for DED fabrication of FGMs.
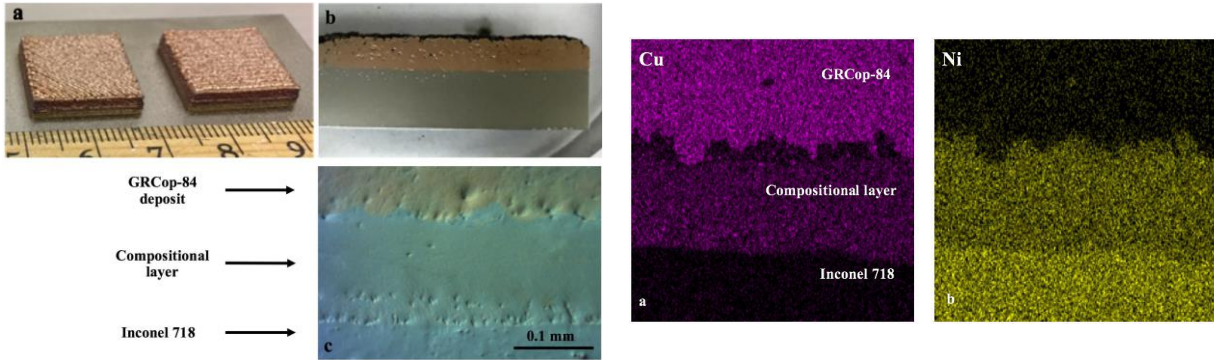
Figure 3. Additive Manufacturing of Inconel 718 – Copper Alloy GRCop-84 Bimetallic Structure using Laser Engineered Net Shaping (LENSTM) (Onuike et al., 2018)
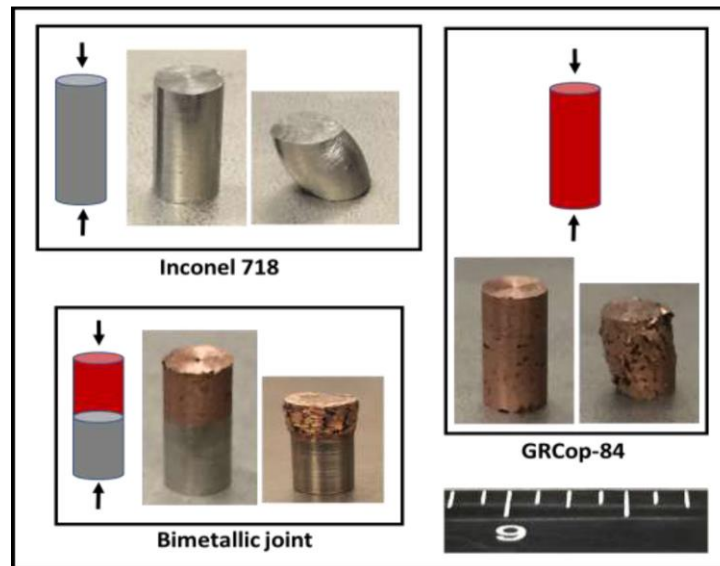
Figure 4. Bond Strength Measurement for Additively Manufactured Inconel 718- GRCop84 Copper Alloy (Onuike & Bandyopadhyay, 2019)

For the FGMs of nickel and copper alloys, Onuike et al. (2018) conducted a study on preblended powders of Inconel 718 and GRCop-84, a copper-based alloy (Figure 3, Figure 4). Two FGMs were fabricated: a straight joint of 100% Inconel 718/ 100% GRCop-84 and a gradient FGMs including 3 levels: 100% Inconel 718, 50% Inconel 718/ 50% GRCop-84, and 100% GRCop-84. Sun et al. (2020) simulated the manufacturing of Inconel 718 and Cu10Sn FGMs using a multi-material powder bed fusion system. The authors investigated thermal-fluid behaviors and the impact of different powder bed configurations (mixed, unmixed, and subcases) on the dynamic of the melt pool via a multi-phase mesoscopic.

As copper and nickel was previously stated to be highly compatible with each other (Karnati et al., 2015), nickel became a potential solution to address the mismatched properties between copper and iron and its alloys. An interesting approach was proposed by Zhang et al. (2021) to use Inconel 718 as interlayers for the fabrication of copper and SS316L. It was concluded that the specimen was successfully manufactured with excellent interfacial bonds at the bi-material surfaces.

2.1.4. Literatures on metals FGMs excluding copper, nickel, and their alloys

Shen et al. (2016) presented the fabrication of iron-aluminum FGMs via wire-arc AM or wire-based DED. On the other hand, Ostolaza et al. (2021) conducted a study on functionally graded SS316 and hot tool steel H13 (AISI H13) using in-situ powder flow-controlled DED. The FGM's gradient ranged from 100% SS316 to 100% AISI H13 with 20% wt increment. Yin et al. (2018) combined the process of SLM and cold spraying to manufacture Al-Ti6Al4V FGMs.

Table 2. Relevant reviewed literatures on metallic FGMs

No.	Literature Reviewed	Process	Materials
1	Chaudhary et al. (2020)	In-situ gradient DED (controlling powder flow)	• Co(100-x)Fe(x) • Ni(100-x)Fe(x) x=[30,70] alloys
2	Dubinin et al. (2021)	In-situ gradient DED (controlling powder flow)	SS316L and Cu-12Al-2Fe
3	Mikler et al., (2017)	Blended powder DED	Fe-30 at %Ni, permalloys of the type (1) Ni-Fe-V and (2) Ni-Fe-Mo, and (3) Fe- Si-B-Cu-Nb
4	Shen et al. (2016)	In-situ Wire-Arc AM	Fe and Al
6	Sun et al., (2020)	Simulation of multiple material laser powder bed fusion	Inconel 718 and Cu10Sn in different power bed configurations to study the melt pool dynamic and thermal-fluid behaviors
7	Ji et al., (2020)	In-situ gradient DED (controlling powder flow)	Ti-6Al-4V and Inconel 718 • 5 layers Ti-6Al-4V 100% • 2 layers 90%Ti-6Al-4V • 1 layer 10%In718 • 2 layers 80%&20% • 2 layers 70%&30% • 4 layers Inc718 100% •
8	Kim et al. (2021)	In-situ gradient DED (controlling powder flow)	Inconel 718 and SS 316L • 11 levels (12layers/level) from 100% Inc718 to 100% SS316L.
9	Zhang et al. (2021)	In-situ gradient DED (controlling powder flow)	SS316L and Cu with Inconel 718 interlayers.
10	Yarrapareddy et al. (2006)	Blended powder DED	Nickel and Tungsten
11	Makarenko & Shishkovsky (2020)	Straight joint DED	Steel and Bronze
12	Makarenko et al. (2020)	Straight joint DED	SS316L and Aluminum Bronze with 10%Al and 1%Fe

13	Ostolaza et al. (2021)	In-situ gradient DED (controlling powder flow)	SS316L and Tool steel H13 • 100% SS316L to 100% H13 • 20% wt intervals
14	Chen & Liou (2018)	Review paper	
15	Karnati et al. (2015)	Blended powder DED	Cu and Ni • 100% Ni to 25% Ni/75% Cu • 25% wt. increment • 100% Cu omitted due to machine limits
16	Yan et al. (2019)	Review paper	
17	Shishkovsky et al. (2016)	In-situ gradient DED (controlling powder flow)	Diamalloy 1005 (Nickel-based alloy) and Al
18	Koizumi (1997)	Review paper	
19	Singh et al. (2017)	Review paper	
20	Lin et al. (2006)	In-situ gradient DED (controlling powder flow)	Cu and Ni • Dual powder system • Wire-powder system
21	Carroll et al., (2016)	In-situ gradient DED (controlling powder flow)	Inconel 625 and SS 304L
22	Yao et al. (2021)	In-situ gradient DED (controlling powder flow)	Stellite-6 and Inconel 718
23	Onuike et al. (2018)	Blended powder DED	Inconel 718 and GRCop-84 • Straight joint • Compositional gradient
24	Yadav et al. (2020)	Blended powder DED	Cu(x) and Ni(100−x) • x = 25, 50, and 75
25	Meng et al. (2020)	DED and laser synchronous preheating	Inc625 and SS316L • 100% Inconel 625 to 100% SS316L • 10% wt. intervals
26	Yin et al. (2018)	SLM & Cold spraying	Al and Ti6Al4V
27	Ghanavati et al. (2021)	In-situ gradient DED (controlling powder flow)	SS316L and Inconel 718
28	Zhang & Liou (2019)	Blended powder DED	SS316L and Inconel 625
29	Articek et al. (2013)	Blended powder DED	Cu and H13 tool steel
30	(Yang et al., 2022)	Blended powder DED	Inconel 718 and SS316L • Straight joint

			• 10% compositional gradeitn from 100% Inconel 718 to 100% SS316L
			• 25% compositional gradeitn from 100% Cu to 100% H13 steel
31	(Onuike & Bandyopadhyay, 2019)	Blended powder DED	Inconel 718 and GRCop-84 • Straight joint • Compositional gradient

2.2. Research Gap & Motivation

Copper-and-nickel-based gradient materials can be utilized in many industries and applications. Copper-nickel FGMs are expected to possess both materials' advantages, including but not limited to thermal and electrical conductivity, high-temperature withholding, high strength and toughness, and corrosion resistance. Furthermore, copper and nickel have been proven by multiple previous studies to be highly compatible with each other, which aids the manufacturing of alloys as well as the fabrication of their FGMs. Nonetheless, the interactive and bonding behaviors between copper-based alloy CuSn10 and nickel-based alloy Inconel 718 is not clearly understood. It is also desirable to examine the microstructures, properties, including both mechanical and physical, of the resulting CuSn10 and Inconel 718 gradient specimens, as well as the feasibility of manufacturing such FGMs via DED approach using a hybrid manufacturing system.

2.3. Potential Challenges

As the nature of FGMs require the collaboration of multiple materials, the general challenge when conducting research on such topic is the mismatched material properties. The differences between materials create additional work for system set-up and potentially affect the manufacturability as well as the duration of the project. For instance, CuSn10 and Inconel 718 possess different melting temperature, which may result in unmelt clusters or poor surface quality (Karnati et al., 2015; Lin et al., 2006).

Additionally, for this specific combination of materials, there is a concern regarding the similarities of the two chosen materials. A potential solid solution may be discovered as the materials are highly compatible. Due to their high compatibility, powder diffusion can also occur at the interface of the materials. Furthermore, as discussed in the previous sections, joining two dissimilar materials, in this case CuSn10 and Inconel 718, without compositional gradient may cause interfacial defects such as cracks and complex phases, despite the materials being highly compatible.

2.4. Problem Statement

While copper-nickel and their alloys have been proven useful in many industries, including advanced fields such as aviation, space, and marine, the feasibility of additive manufacturing, especially via DED approaches, including parameter optimization and their impact on the quality of the specimens have not been clearly understood. Furthermore, the particular pairing of CuSn10 and Inconel 718, both of which are strengthen alloys of copper and nickel, has not been well presented in the literature in regard to their microstructure, mechanical, and physical properties. Coupled with the desire to investigate such FGM manufacturability via DED approach created motivations for the present thesis to take place.

2.5. Objectives of the Present Thesis

Functionally gradient materials (FGMs) of CuSn10 and Inconel 718 were fabricated via a hybrid directed energy deposition (DED) system. The objective of the present thesis is:

(1) to determine the feasibility of fabricating CuSn10 and Inconel 718 FGMs via DED and

(2) to investigate the physical and mechanical properties and the microstructures of the resulting FGMs.

The physical tests comprised of conductivity and Seebeck coefficient measurements. The microstructure analysis and mechanical testing include microscopic imaging, scanning electron microscopy (SEM), energy dispersive spectroscopy (EDS), and hardness test. In addition, compressive strength test was performed to analyze the interface bonding behaviors.

3. Methodology

3.1. Materials & Equipment

The system utilized for the specimen fabrication of this present thesis was the Hybrid Manufacturing Technology AMBIT Printer (Figure 5, Figure 8). Hybrid manufacturing refers to the combination of additive and subtractive processes in the same system. The additive component of the system is utilized to fabricate parts which later undergo post-processing using the subtractive component. It is common for DED-printed parts to have low surface quality and thus, to require the aid of subtractive machining after the three-dimensional fabrications.
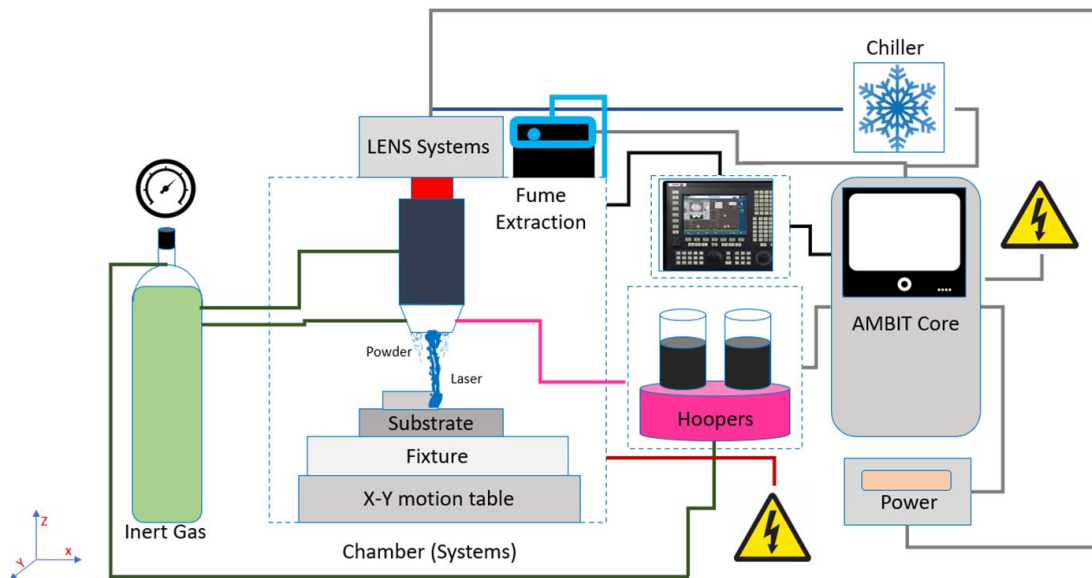
Figure 5. Schematic Diagram of AMBIT System (Era, 2021)
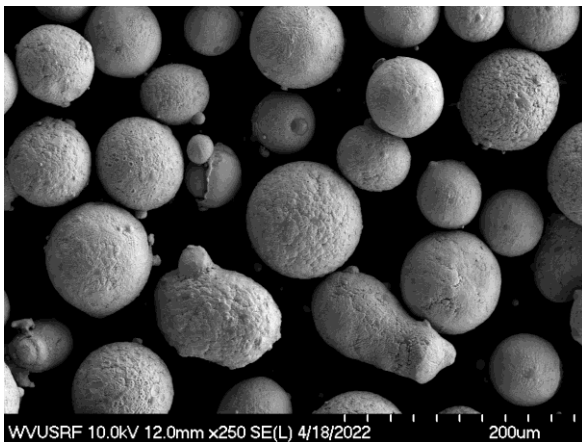
Figure 6. SEM Scan of CuSn10 powder
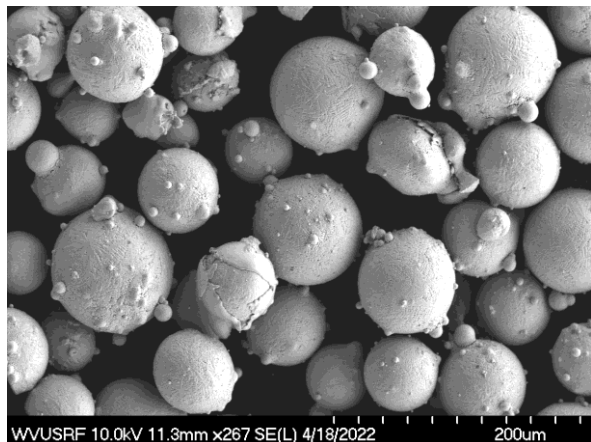
Figure 7. SEM Scan of Inconel 718 powder

Table 3. CuSn10 Chemical Composition (%wt) via MSE Supplies LLC.

Sn	9.2~11.5	**Ni**	≤0.10
Zn	≤0.05	**Al**	≤0.01
Pb	≤0.25	**Fe**	≤0.08
P	0.60~1.0	**Mn**	≤0.05
Cu	Balance		

Table 4. Inconel 718 Chemical Composition (% wt) via Carpenter Additive

C	≤0.08	**P**	≤0.015
Si	≤0.35	**Ti**	0.65~1.15
Mg	≤0.35	**S**	≤0.015
Cr	17.00~21.00	**Co**	1.0
Mo	2.80~3.30	**Fe**	Balance
Al	0.35~0.80	**Cu**	0.15
Nb/Ta	4.75~5.50	**B**	0.001~0.006
Ni/Co	50.00~55.00		

CuSn10 powder with particle size of 45-105 microns (Figure 6) was obtained from MSE Supplies LLC. CuSn10 is a strengthened copper alloy with 10% tint. The chemical composition of this powder was presented in

Table 3. The alloy is discussed to have high strength and springiness due to the added tint, and overall high wear and corrosion resistance (MSE Supplies).

Inconel 718 powder was obtained from Carpenter Additive with particle size of 45-106 microns (Figure 7). The chemical composition for this power was presented in Table 4. Inconel 718 is a high-temperature resistance specialty nickel-based alloy with excellent yield, tensile, and creep-rupture properties. It is also known for chlorides, stress corrosion, and sulfide stress cracking resistance (Carpenter Technology). The FGMs are to be printed on stainless steel (SS316L) substrate.

Figure 8. Hybrid Manufacturing Technology AMBIT DED Printer (top) and its components (bottom)

3.2. Methodology

3.2.1. Parameter Optimization

As mentioned in the earlier part of the thesis, three of the most important process parameters in DED processes are identified to be laser powder, laser scanning speed, and powder feeding rate (Gibson et al., 2014). Hence, an attempt to optimize the three parameters were carried out for the obtained CuSn10 and Inconel 718 powders. The objective of the parameter optimization is to obtain the ideal settings for each powder to ensure a smooth fabrication process and an overall enhanced quality of the printed structures.

Table 5. Potential Parameter Combinations for CuSn10 Powder

No.	*Laser Power (W)*	*Scanning speed (mm/s)*	*Powder feeding rate (g/min)*
a	800	10	9
b	900	10	9
c	700	10	9
d	600	10	9
e	700	10	6
f	700	10	12
g	700	9	9
h	700	9	6
i	700	11	6

The optimized parameters for Inconel 718 powder have been obtained from previous studies using the same system. Such combination of parameters was presented in Table 6.

For CuSn10 powder, the experiments were conducted on a 10mm-by-12mm block. Two layers of materials, each 0.54mm thick, were deposited for each combination. Nine combinations of parameter set-ups (Table 5) were investigated for the parameter optimization of the tint-strengthen copper alloy CuSn10 powder. The combinations were chosen based on trials-and-errors during print. Criterium for quality include a smooth surface quality and an accurate dimensional accuracy, both of which will be graded visually.

3.2.3. Test Sample Preparation Procedures

Using the results obtained from the parameter optimization, a total of six specimens, including four CuSn10-Inconel 718 FGMs, one 100% CuSn10 specimen, and one 100% Inconel 718 specimen, were fabricated and prepared to accommodate the aforementioned testing plan. Layers of Inconel 718 was first deposited atop the SS316L substrate. Subtractive facing was carried out to earn an even and smooth surface for the next CuSn10 region deposition (Figure 9). Power calibration procedure was also performed in-between each material change-over to prevent trapped wasted powder from forming defects.

CuSn10 was then printed atop the processed Inconel 718 region. As the CuSn10 zone was fabricated at a higher latitude compared to the Inconel 718 region, which was deposited atop the substrate, the offset between the printhead and the specimen became relatively small. In order to protect the LENS equipment, the process was monitored closely and override if the offset reduced below the safe threshold. After every stop, the top surface of the specimen was inspected. If required, subtractive facing was carried out before the next deposition. For this reason, subtractive procedures were required not only in between material regions but also within each region.

Figure 9. Example of fabrication process (Inconel 718): pre-facing specimen (top) and post-facing specimen (bottom).

Upon the successful fabrication of both regions of the FGM (Figure 10), another facing attempt was performed to achieve a smooth and high-quality top surface in preparation for testing procedures (Figure 11). As the specimens were to be cut into samples, there was no need for contouring along the length of the specimen. If a smooth surfaced along the length of the specimen was required, such quality could be achieved via laying off the rough edges using the precision cutting tool (Figure 12).
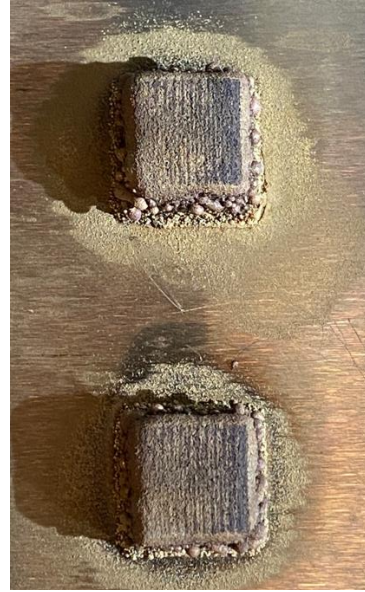
Figure 10. Fabricated CuSn10-Inconel 718 FGMs

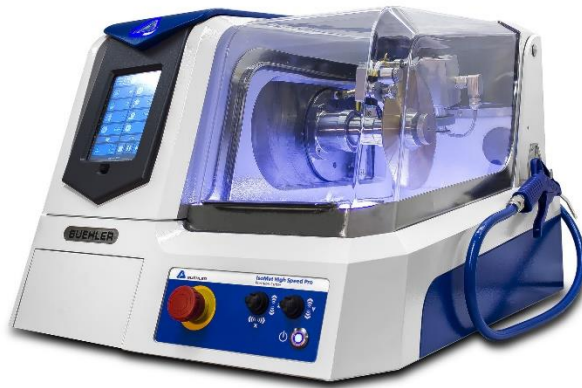*Figure 11. CuSn10-Inconel 718 FGM Post-facing*

Figure 12. Buehler IsoMet High Speed Pro precision cutter (shop.buehler.com)

In order to provide consistent results throughout the plan, FGM test samples, excluding the cylindrical sample, were cut from one single CuSn10-Inconel 718 specimen (Figure 13), which had the original dimensions of 15mm-by-15mm-by-15mm, using the Buehler IsoMet High Speed Pro precision cutting tool (Figure 12).

A sample measured 5mm-by-9mm-by-14mm were obtained to accommodate hardness test. This sample was later further sectioned down to 5mm-by-5mm-by1.8mm and prepared again to undergo SEM and EDS analyses (Figure 14).

Another sample (measured 4mm-by-4mm-by-11mm) were utilized for conductivity and Seebeck coefficient change measurements. Two single-material samples, both measured 4mm-by-4mm-by-11mm, were produced from the 100% CuSn10 and 100% Inconel 718 specimens to accommodate the same measurements (Figure 15).
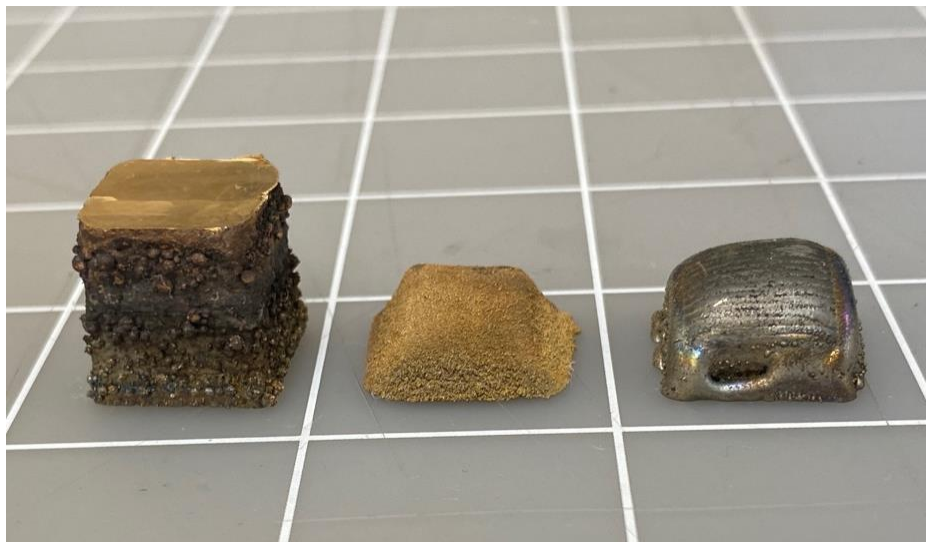

Figure 13. Original specimens to be cut for testing procedures. From left-right: CuSn10-Inconel 718 FGM, CuSn10 specimen, Inconel 718 specimen
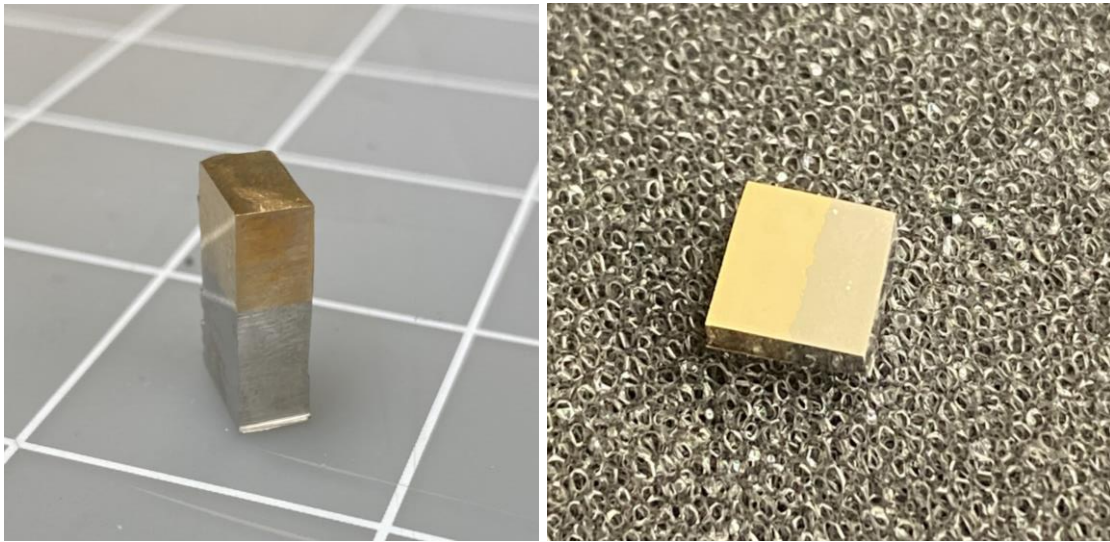
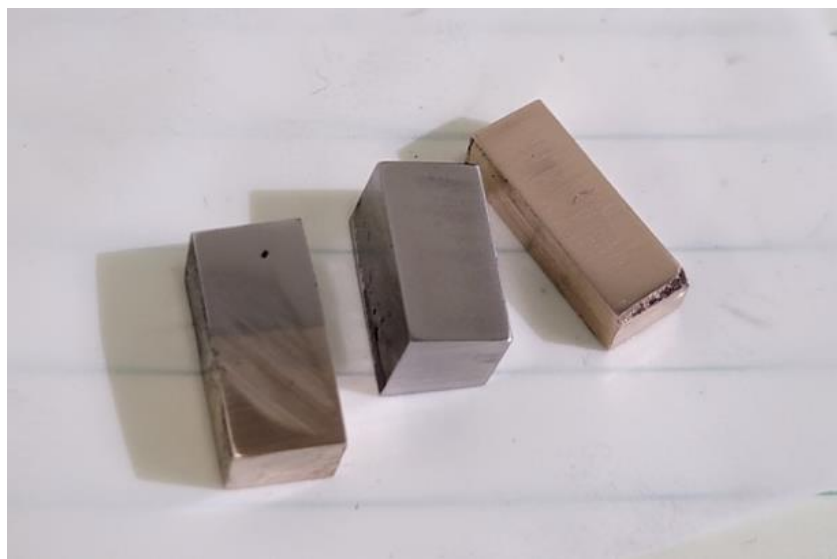*Figure 14. Hardness test specimen (left) and SEM/EDS/Microscopic-imaging specimen (right)*

Figure 15. Conductivity & Seebeck coefficient changes specimens
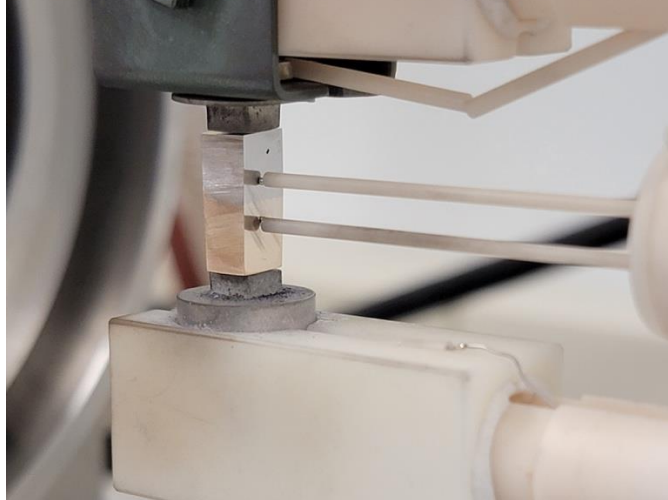*(left-right: FGM, Inconel 718, CuSn10)*

Figure 16. Conductivity & Seebeck coefficient measurements

Lastly, a cylindrical FGM of CuSn10-Inconel 718 were fabricated with a diameter of 15mm and height of 22mm (Figure 17a). The same procedures of additive-substrative was applied to the fabrication of this specimen. As the specimen had a larger height than the cube specimens, the offset created more stops and starts. For that reason, facing in-between prints was required more often.

Inconel 718 was repeatedly deposited and faced until a final height of 12mm (measured with a flat top surface) was achieve. The same steps were repeated for CuSn10 until a final height (measure with a flat top surface) of 10mm was achieved. The different between the final height of the regions reflected a safety cushion for Inconel 718 as it was printed atop the substrate. In order to prevent loss of materials when severing the specimen from the substrate, more Inconel 718 were printed.

Upon the successful additive manufacturing of the cylindrical FGM, contouring was conducted along the length of the specimen using the subtractive component of the AMBIT system. In contrast to the cubic specimens whose rough edges could be easily severed from the parts using the precision cutting tool, due to the circular shape, subtractive contouring must be carried out to earn a smooth all-around surface quality for the cylindrical FGM. Its diameter was reduced to 12mm after this process (Figure 17b).

The first attempt of compressive strength test was carried out with this specimen (d=12mm). However, after recognizing the failure of such test, the specimen was turned to achieve a smaller, more suitable diameter of 5mm (Figure 17c). The height of the specimen remained 22mm, where the height of CuSn10 region measured 10mm and that of the Inconel 718 region 12mm, throughout the substrative manufacturing process. The specimen underwent compressive strength test once more to evaluate the surface bonding behaviors of the two materials.
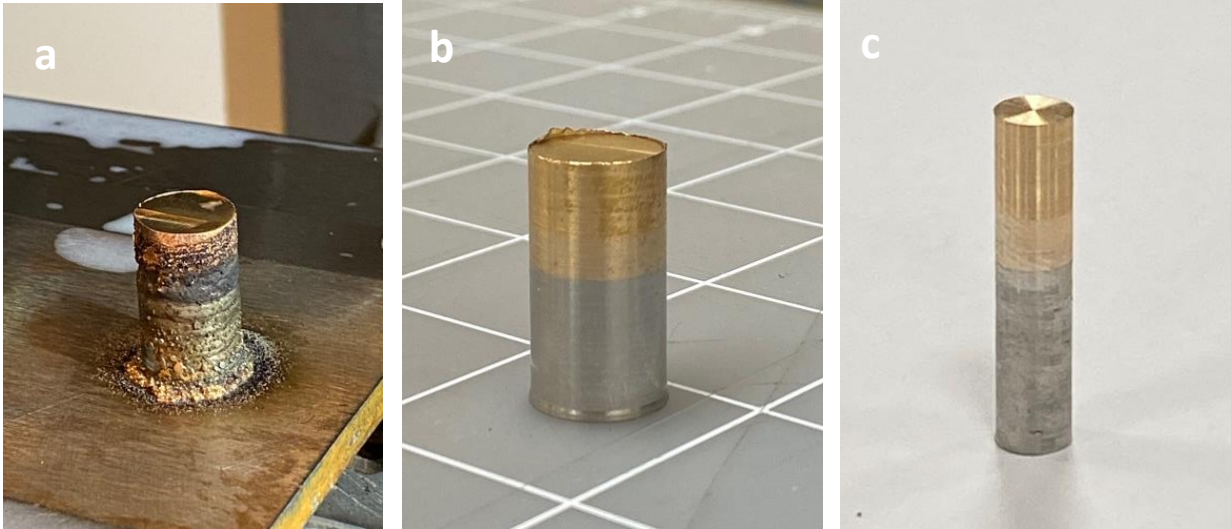
Figure 17. Cylindrical specimen for compressive strength testing through the steps: (a) fabricated, pre-machining, (b) post-machining. (c) post-turning.

3.2.4. Testing Set-up

Following the sectioning of the samples, as the required dimensions for each test was achieved, the samples were grinded and polished (Saphir 250 A1-ECO, Mager Scientific, United States). The samples were cleaned using alcohol and cotton balls in order to ensure no new scratches or surface defects occurred.

Microstructure analysis was conducted via a scanning electron microscope equipped with energy-dispersive x-ray spectroscope (S4700, Hitachi, Japan). A silver paste was used to mount the sample to the holder with no other coating nor additional processing. An accelerating voltage of 15kV and a beam current of 10µA was applied for both SEM and EDS analyses.

Hardness across the surface of the sample was measured using a Vickers hardness tester (Model 900-390, Phase II+, United States). A load of 9.980N was applied for a duration of 15 seconds for each measurement. A total of 51 data points were obtained from the test procedure. At the interface of CuSn10 and Inconel 718, nine measurements were taken. For each zone of CuSn10 and Inconel 718, 21 measurements were taken. The measurement mapping can be found in Appendix 1.

Conductivity and Seebeck coefficient changes analysis were carried out using a measuring device for thermoelectric (LSR-1100, Linseis, Germany) following the four-terminal method (Figure 16). The measurements were performed in the temperature range of approximately 313K to approximately 383K. The environment was a low pressure He environment.

Compressive strength test was conducted on a universal tester (AGS-X, Shimadzu, Japan) with 10kN compressive load and the testing speed of 1.5mm/min to investigate the bonding behaviors at the interface of the FGM. The specimen diameter and length were 5mm and 22mm, as reported in the previous section, respectively. Stress and stroke data was collected simultaneously.

4. Results & Discussions

4.1. Parameter Optimization

At laser power of 800W, scanning speed of 10mm/s, and powder feeding rate of 9g/min (Figure 18a), the fabricated specimen showed good surface quality and relatively comparable dimensional accuracy. There was proof of metallurgical bonding between the layers and between the first layer and the substrate. The laser power was chosen as the first parameter to be studied while scanning speed and powder feeding rate were fixed at 10mm/s and 9g/min, respectively.

At 900W, the produced specimen (Figure 18b) had higher layer height and lower dimensional accuracy when compared to the specimen produced previously at the lower temperature. It was concluded that fabricating specimens at a higher laser powder was more time and material consuming with no improvements to the overall quality of the finished parts. Therefore, no higher laser power was tested.

At 700W, the produced specimen (Figure 18c) had the highest surface quality and dimensional accuracy out of the three tested combinations. It was hypothesized that as the laser power was decreased, the overall quality of the specimen increased. Thus, laser power was lower to 600W to examine this theory. However, when the laser power lowered, so did the dimensional accuracy (Figure 18d). Hence, the laser power was kept constant at 700W, where the best overall quality specimen was produced.

Additionally, it was observed that at the feeding rate of 9g/min, the layer thickness was relatively high. Hence, while laser power was fixed at 700W and scanning speed at 10mm/s, the feeding rate was varied. First, it was lower to 6g/min. The produced specimen (Figure 18e) has the best overall quality in all of the printed specimens, though relatively comparable to the specimen 9g/min with the same laser power and scanning speed.

Moreover, at the feeding rate of 6g/min, the layer thickness was significantly lower. No lower feeding rate was tested for a lower layer height was not desired. When the feeding rate was instead increased to 12g/min, the dimensional accuracy was compromised, thus, prompting no further increasement to the feeding rate (Figure 18f). Between the feeding rate of 6g/min and 9g/min, the produced specimens showed comparable overall quality, hence, to minimize powder consumption, the lower feeding rate was chosen as the optimal option.

Two additional scanning speeds of 9mm/s and 11mm/s were tested. First, two specimens were printed using the scanning speed of 9mm/s. One of them was produced at laser power of 700W and feeding rate of 9g/min (Figure 18g). The second was produced at the same laser power but a lower feeding rate of 6g/min (Figure 18h). At the higher feeding rate, the specimen (Figure 18g) displayed comparable surface quality but slightly lower dimensional accuracy. Hence, for scanning speed of 11mm/s, only one combination with feeding rate of 6g/min and laser power of 700W was tested. The printed part (Figure 18i) has comparable dimensional accuracy and surface quality to its counterparts yet a slightly lower layer thickness.
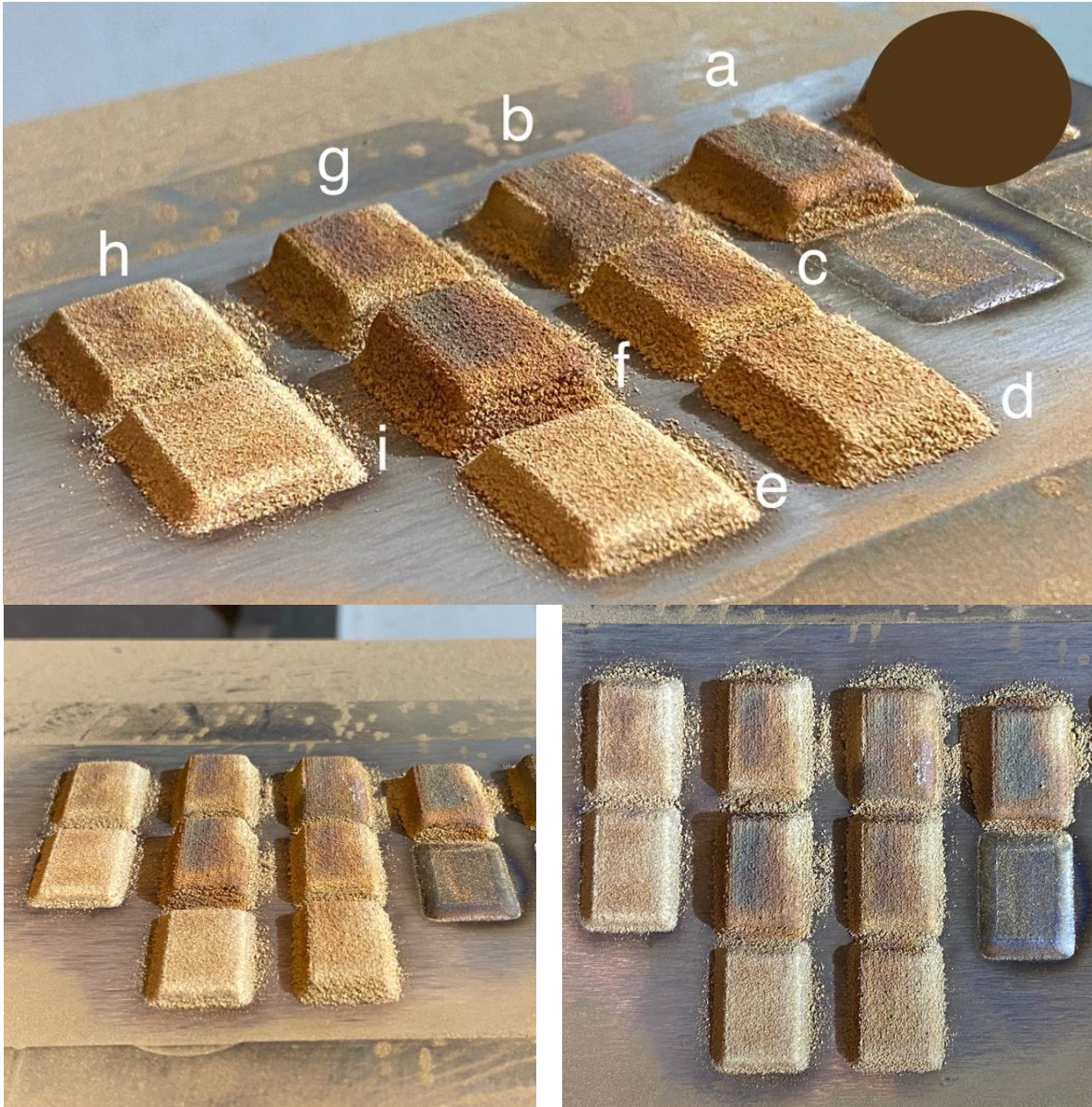
Figure 18. Specimens from CuSn10 parameter optimization process

Overall, all of the printed specimens displayed a very good surface quality as well as dimensional accuracy. Based on the overall visible quality and layer thickness, the specimen produced using the combination of 700W laser power, 10mm/s scanning speed, and 6g/min powder feeding rate was rated highest (Figure 18e). Hence, the parameter combination was recorded and applied to fabricate the present thesis' specimens (Table 6). This particular parameter combination also reflected a minimized power and material consumption.

| Optimized Parameter	CuSn10	Inconel 718
Laser Power (W)	700	900
Scanning Speed (mm/s)	10	10
Powder Feeding Rate (g/min)	6	5
Layer Thickness (mm)	0.54	0.54

4.2. Microstructure Analyses

Figure 19 exhibits the microscopic images captured at the interface of the CuSn10-Inconel 718 FGM. It can be observed from the images that there was a defined interface with clear separation between the regions of CuSn10 and Inconel 718. Additionally, evidence of metallurgical bonding between the two materials can also be detected from the same images.

Nonetheless, it is important to highlight that the interface of the two materials did not appear to be smooth. Moreover, CuSn10 particles can be observed within the Inconel 718 region and vice versa. The previous findings can be taxed on the material diffusion between CuSn10 and Inconel 718 as copper and nickel were aforementioned to be highly compatible with potential solubility. The diffusion between the two materials created a complex interface which inherently resulted in varying properties at the interface of the FGM. Furthermore, due to the diffusion, there could be a secondary phase formation at the interface of the FGM. However, further testing must be conducted to identify the potential secondary phase.
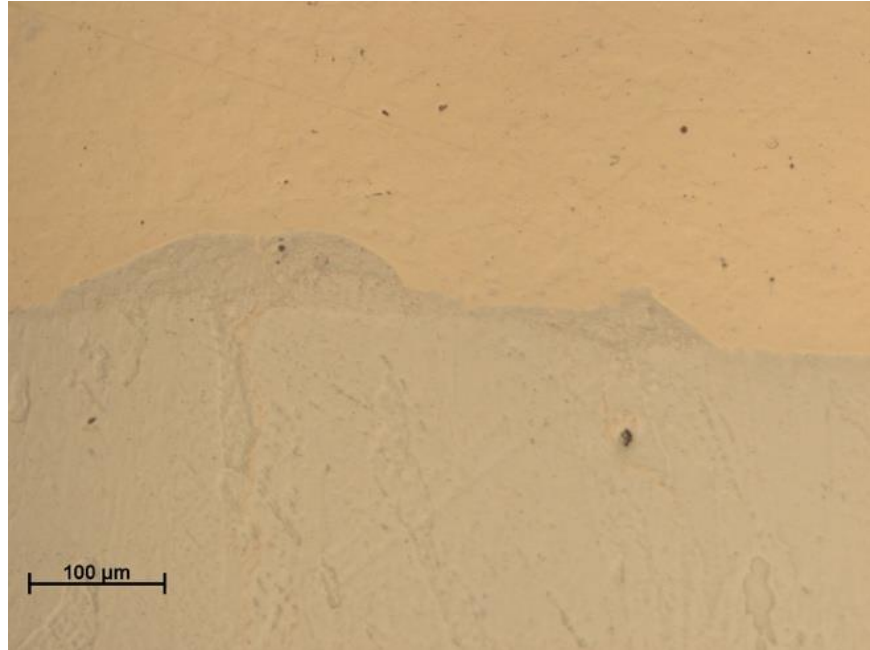

200 μm
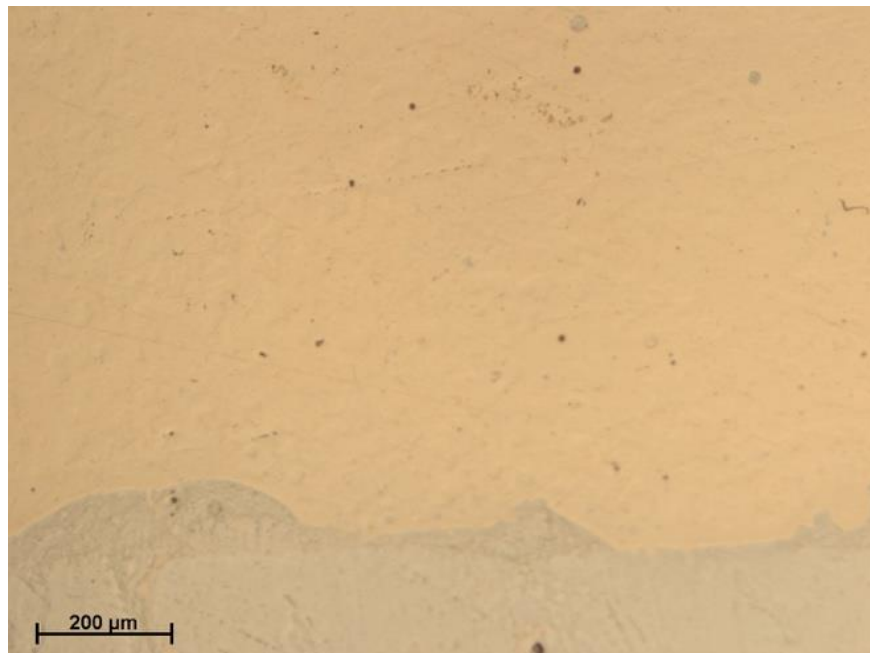
Figure 19. Microscopic images of the FGM interface

In addition, porosity could be detected in both material regions. Pores identified in the Inconel 718 regions were larger in size compared to those in the CuSn10 region. Porous microstructure resulted primarily from trapped air during the fabrication process. The same defects were also observed by Karnati et al. (2015) and Yadav et al. (2020) in their continuous Cu-Ni FGM fabricated via preblended powder DED. A potential crack caused by solidification shrinkage at the surface of the Inconel 718 region might add to the diffusion effect (Figure 20, Figure 21). Joining two dissimilar materials without compositional gradient has been discussed to be the cause of interfacial problems such as cracks or delamination (Yang et al., 2022).
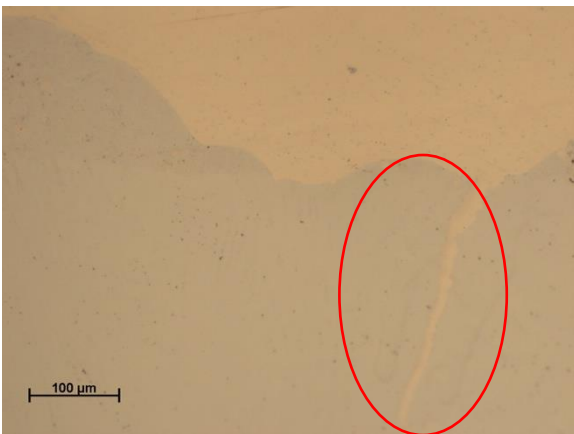
Figure 20. A potential crack identified via microscopic imaging
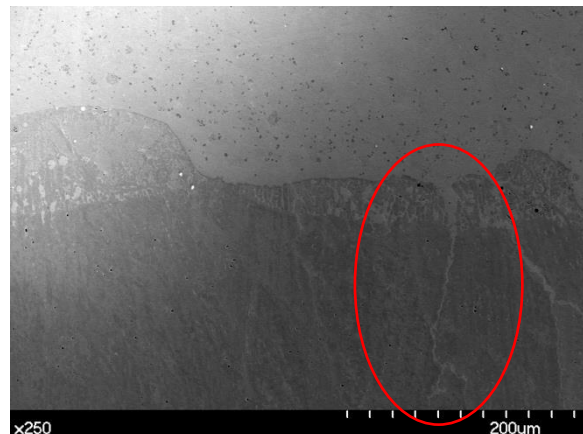
Figure 21. A potential crack further verified via SEM images
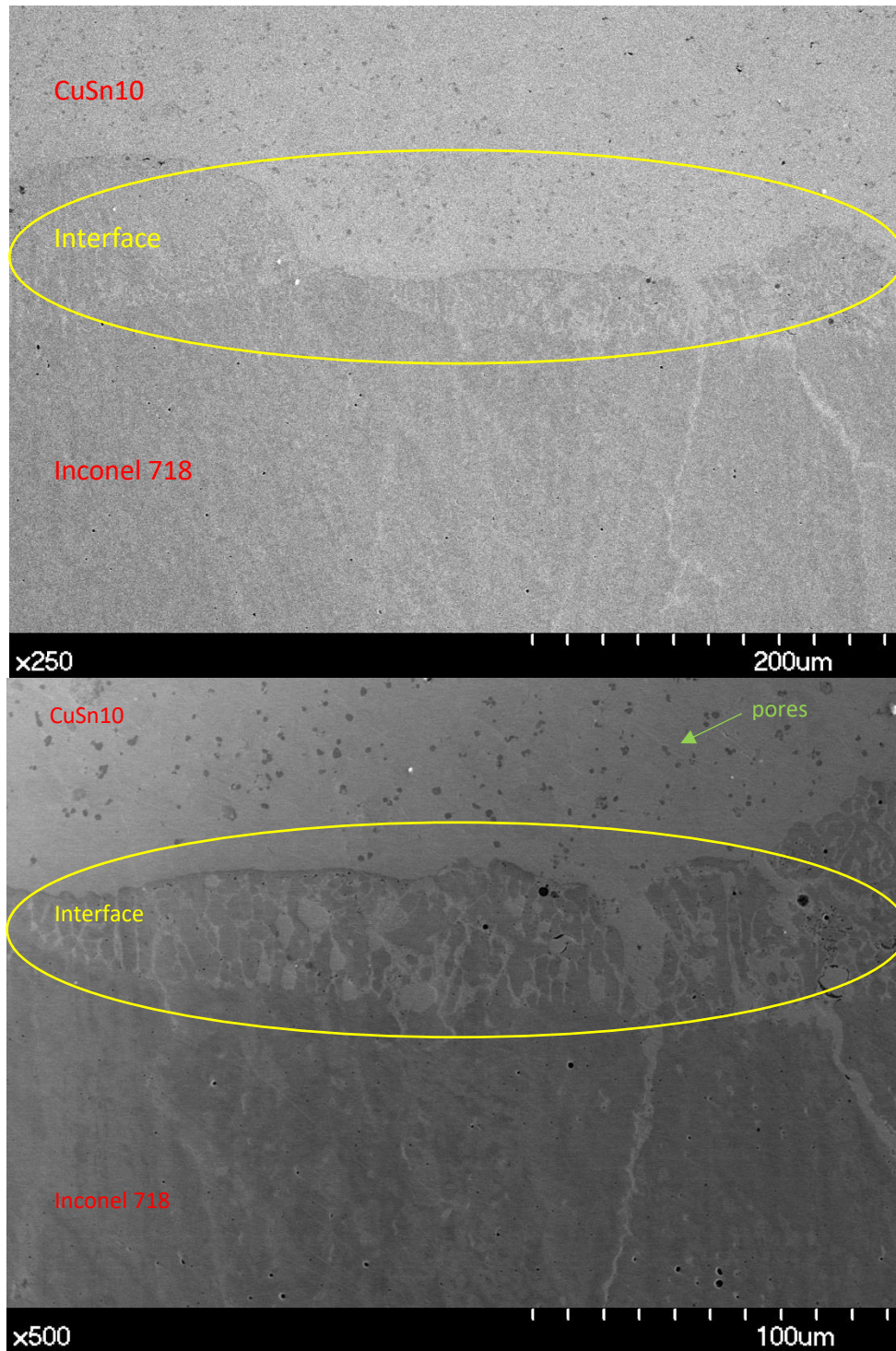
Figure 22. SEM results at the FGM interface

Images from SEM further validate the aforementioned findings. It could be remarked clearly from Figure 22 the defined regions of the FGMs. The diffusion of CuSn10 and Inconel 718 formed a middle layer in between the two single material regions. Inconel 718 particles were detected in the CuSn10 region and vice versa. Porosity microstructure was observed. The images obtained from the SEM can be compared to those showcased in Figure 3. In the image provided by Onuike et al.

(2018), three different regions could be identified, enriched GRCop-84, fused powder interface, and enriched Inconel 718.

Figure 23 showcases the results from EDS. CuSn10 and Inconel 718 were identified at the surface. Observations also showed CuSn10 penetrating into the Inconel 718 region and vice versa. Additionally, enriched Mo and Nb could be detected with a potential formation of a secondary phase with CuSn10. Cr-enriched particles were also identified in the CuSn10 region. The finding reflected and confirmed the presence of additional metal such as Mo, Nb, and Cr in the Inconel 718 composition as was presented in earlier part of the thesis.
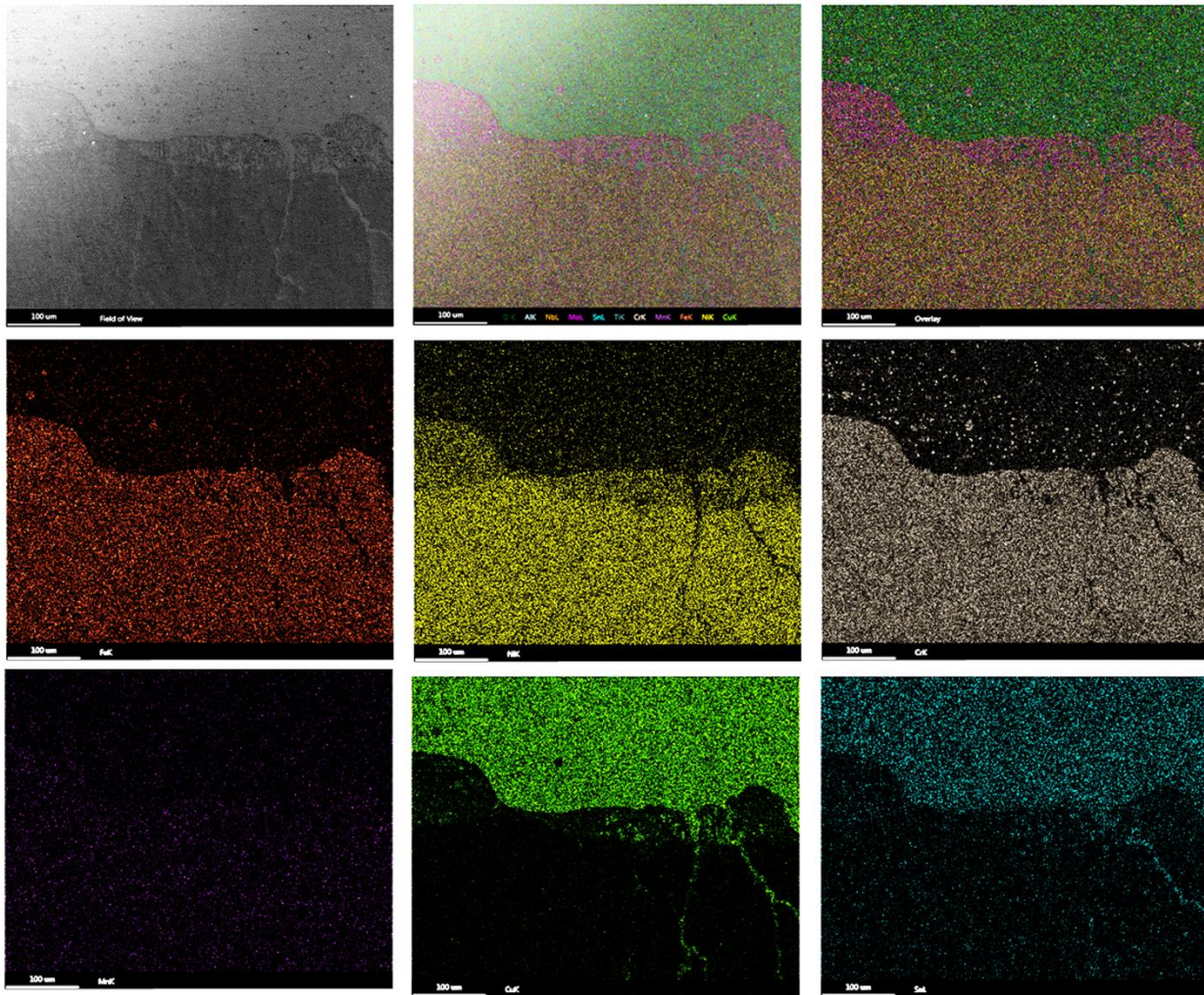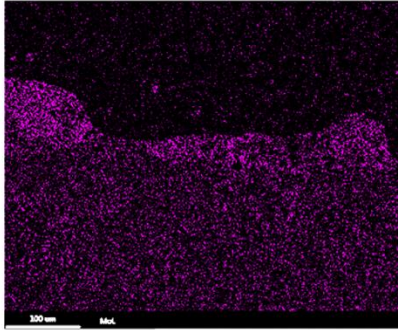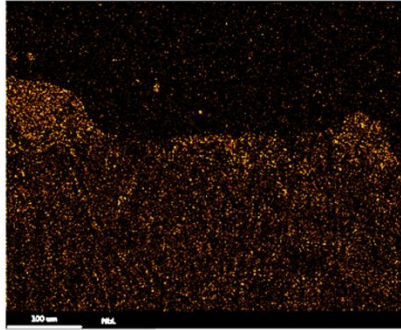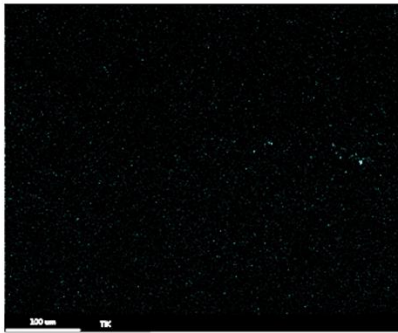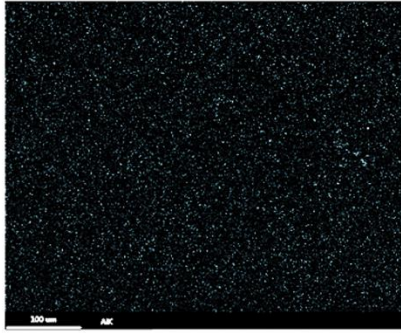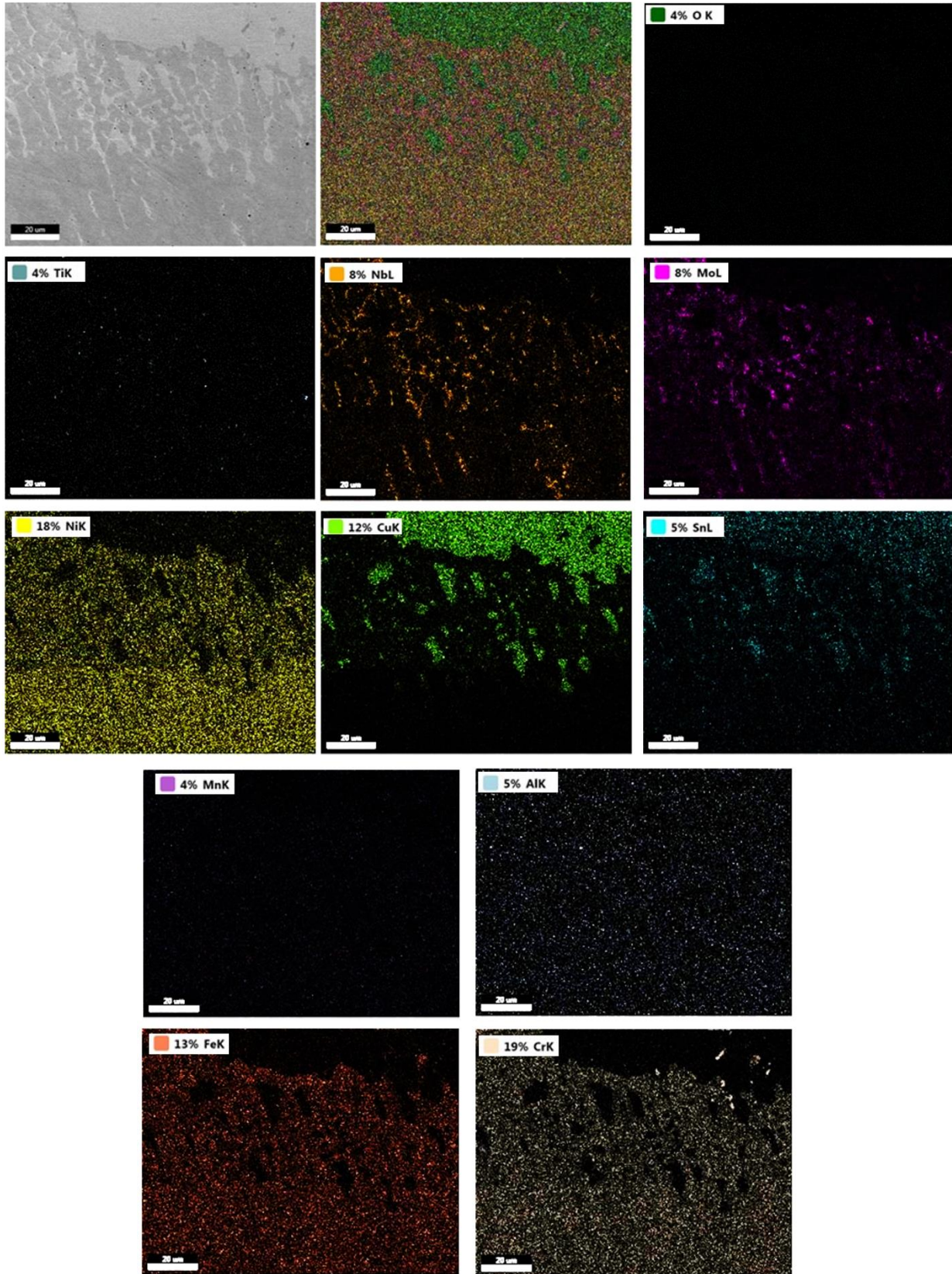
Figure 23. EDS results at the FGM interface

4.3. Vickers Hardness Test

The raw hardness data was observed for outliers which contained seven data points in the CuSn10 zones. The omitted seven measurements showed a significantly lower hardness due to a tilt in the surface, resulting in the data being taken at an angle. Figure 24 exhibited the hardness profile of the CuSn10-Inconel 718 specimen. Hardness in the CuSn10 zone was measured within a distance of 2 mm from the interface of the two materials [1mm, 2mm] while hardness in the Inconel 718 zone was measured within a distance of 3 mm from the intersection [-3mm, -1mm]. For a measurement mapping, refer to Appendix 1.

Hardness was remarkably different across the regions of the FGM (Table 7). The hardness measured in CuSn10 zone was significantly lower in comparison to the rest of the specimen. The findings were consistent with the known characteristic of copper and nickel. Copper is a softer material often utilized for ductility applications while nickel is well-known for its strength and toughness. While the material studied in the present thesis were alloys, the majority of the weight distribution was still copper and nickel.

Table 7. Hardness Test Results

Zone	Mean	Std. Deviation	Min	Max
CuSn10	135.15	6.10	135.20	143.70
Interface	220.54	32.33	160.60	661.10
Inconel 718	270.74	13.91	241.90	292.40

The hardness measured at the interface of the FGM reflected an improvement compared to the CuSn10 region. As previously discussed, FGMs inherit the characteristic of both materials, allowing them to outperform single-material counterparts. In this case, the presence of Inconel 718 enhanced the hardness at the interface of the FGM.

Furthermore, there appeared to be a steep decrease in hardness of the CuSn10 region from the interface of the FGM. Figure 24 showcased a significant drop as departing from the interface towards the CuSn10 region. This result was consistent with that discussed by Onuike et al. (2018). It was stated that there was a sharper transition in the hardness across the direct-deposited, or in other words, stepwise GRCop-84-Inconel 718 FGM where it increased as departing from the GRCop-84 zone towards the interface and the Inconel 718 zone, when compared with the compositional gradient FGM. The same findings were also reported by Yadav et al. (2020). The authors mentioned that with a sharp transition of materials appeared a steep increase in the hardness. Gradient layers were discussed to help with this abrupt change.

A previous study on GRCop-84 and Inconel 718 done by Onuike et al. (2018) reported a value of 140.7±4.079HV for their GRCop-84 region, approximately similar to the values obtained for CuSn10 in the present thesis. For Inconel 718, the same authors denoted a value of 298.8±6.118HV. Although the hardness reported was in the approximate range with values measured from the CuSn10-Inconel 718 FGM, the lower hardness in our sample could be caused by the different parameter set-up for both studies. Nonetheless, no hypothesis testing was carried out to confirm the difference between the mean of the two results.
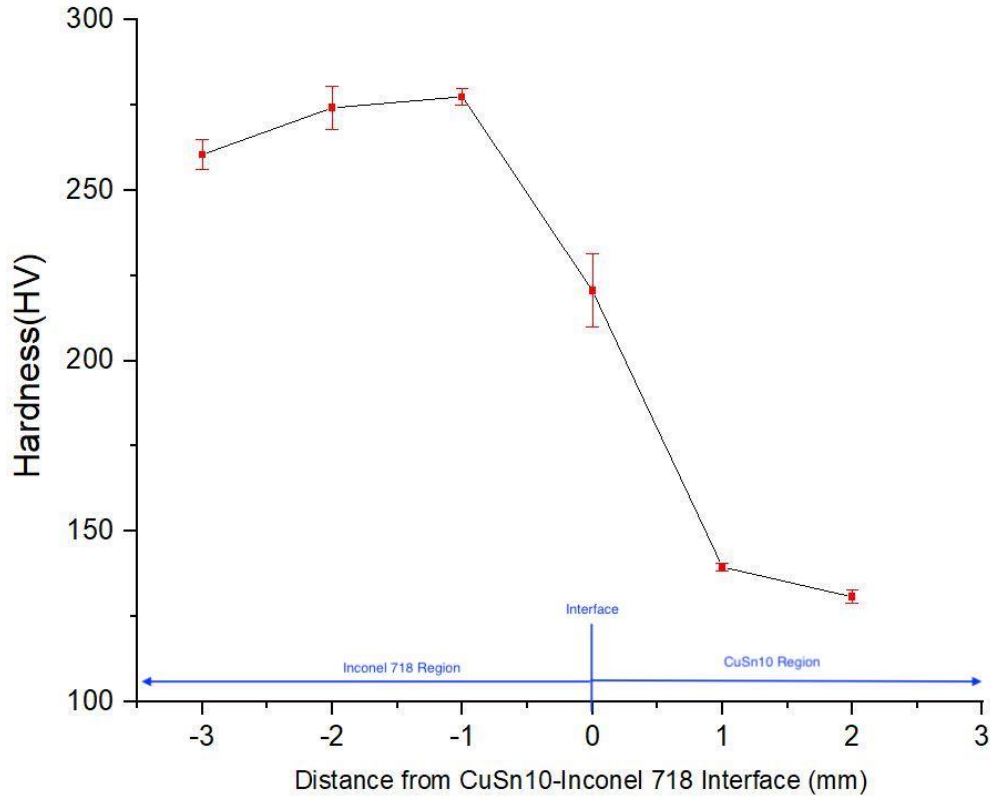
Figure 24. Hardness across the FGM

On the other hand, with regard to their pure copper-nickel FGM, Yadav et al. (2020) discussed hardness of Cu region to be 49 to 55 HV and as-deposited Ni shows microhardness of 99 to 105 HV. Both of the regions show significantly lower hardness in comparison to the present thesis and the study by Onuike et al. (2018). It was believed that this is due to the fact that Yadav et al. (2020) utilized pure copper and nickel material in their research while the present author and Onuike et al. (2018) studied their alloys, which might be strengthen and improved.

The high variability of values measured at the interface of the FGM (Figure 12, Zone B) was influenced by material diffusion explained via microstructure analyses. As elucidated in the earlier section of the present thesis, penetrations of one material into the other region resulted in a complex interface where properties of the FGM reflected those of both of its materials, leading to high variation.

In order to further explore the impact of the diffused layer, additional hardness test coupled with SEM scanning and microscopic imaging of the indented sample was conducted. The mapping and results from this additional hardness test can be found under Appendix 2. A total of 21 measurements were, where seven data points belong in the interface of the FGM and seven data points belong in each single material zone, measured within a distance of 1.5mm of the interface. Figure 25 displayed the microscopic image obtained from the hardness-indented sample. Mark number 1 to 7, 8 to 14, and 16 to 22 exhibited the indentations in the CuSn10 zone, the interface, and the Inconel 718 zone, respectively. Mark 15 was a test indentation where no hardness data was obtained.

It is important to highlight that while taken in the approximate location of the interface, the indentations in this region displayed different qualities due to the effects of material diffusion and penetration (Figure 26). Mark 13 covered three different regions: CuSn10, interface, and Inconel 718 while Mark 9 and 11 were taken right at the interface of the FGM. On the other hand, Mark 8 and 10 were taken in the newly form secondary phase involving Inconel 718, displaying a significantly higher hardness at 278.7 and 298.1 HV, respectively. Opposite to Mark 8 and 10, Mark 12 and 14 were observed within the newly formed secondary phase involving CuSn10. This finding further explained the notably lower hardness obtained from these two indentations (236.8 and 262.7, respectively). The discussed findings were further validated using SEM scannings (Figure 27).
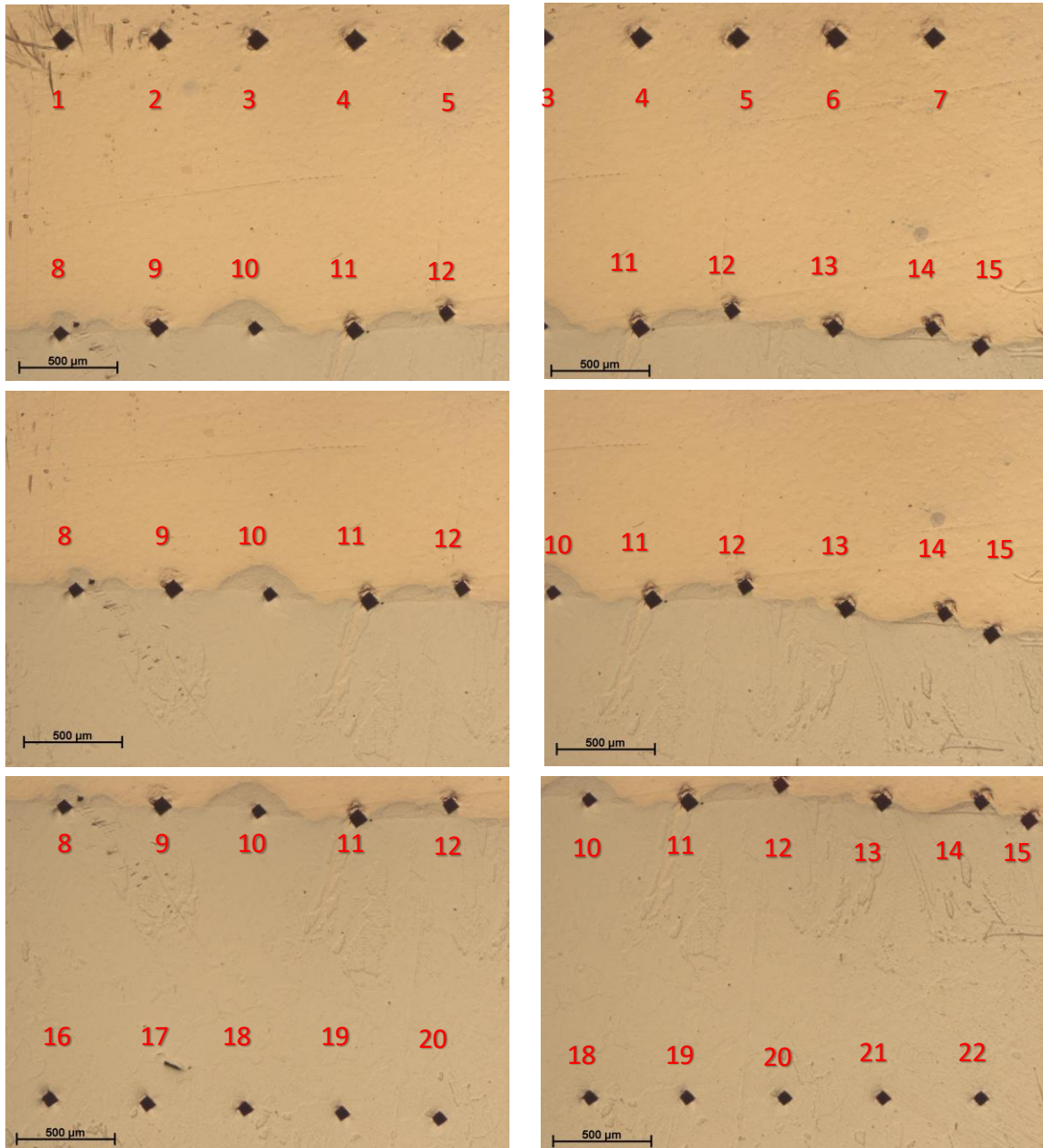
Figure 25. Microscopic image of the hardness-indented specimen
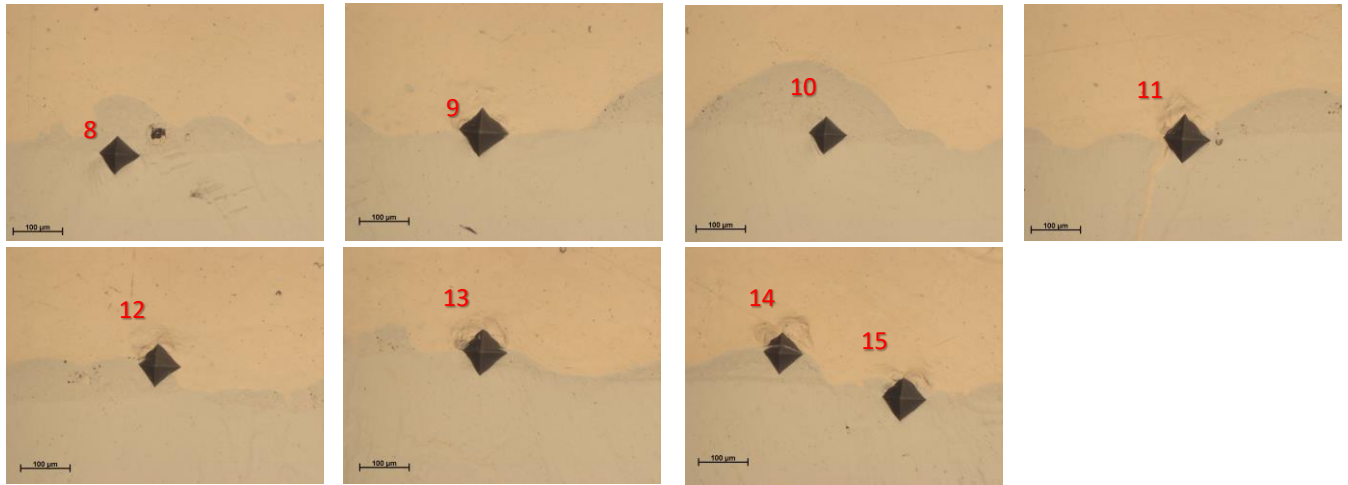
Figure 26. Hardness indentations 8-15 taken at the interface of the FGM
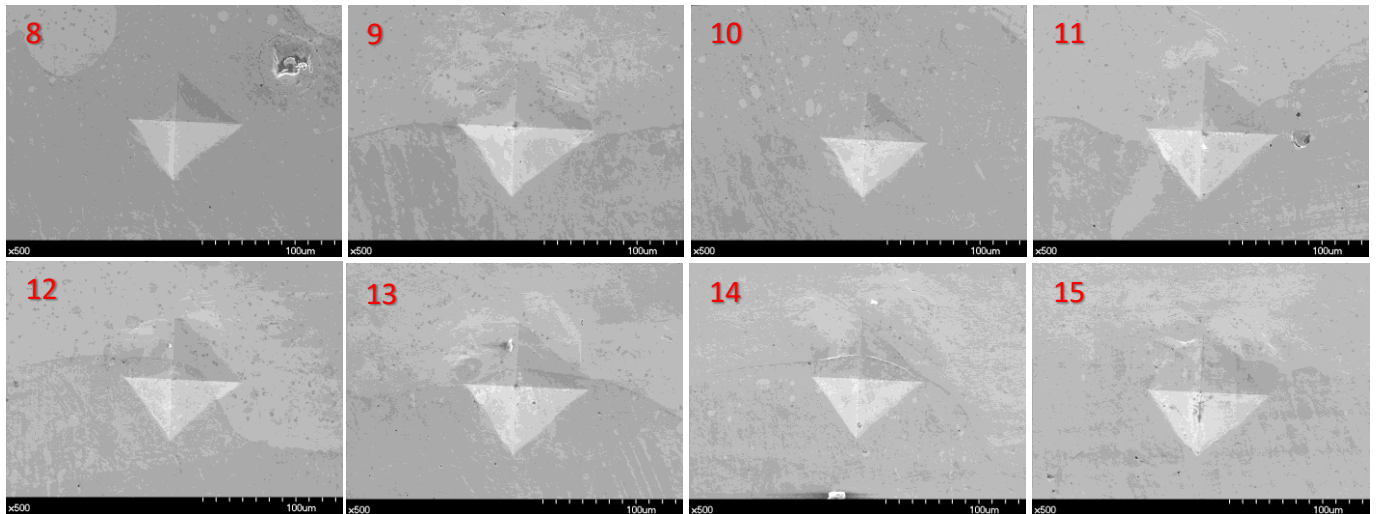
Figure 27. SEM results from hardness indentations at the interface of the FGM

4.4. Conductivity & Seebeck Coefficient Change Analysis

The analysis displayed evidence that electrical conductivity and the Seebeck coefficient changes were induced by the interface of the CuSn10 and Inconel 718. Figure 28 demonstrates the electrical resistivity of the three samples. Among the three samples, in the temperature range of 320 to 390K, CuSn10 displayed the lowest electrical resistivity, or in other words, the highest electrical conductivity, while Inconel 718 the lowest.

The electrical resistivity of the FGM measured from the interface of the two materials was observed to be in the middle of this range. The finding further validating the previous discussion on the inheritance effect of FGM. While Inconel 718 allowed for a higher hardness at the interface of the FGM, CuSn10 improves the electrical conductivity.

34

Figure 29 presented the results from the Seebeck coefficient change analysis. The CuSn10-Inconel 718 FGM displayed the highest absolute Seebeck coefficient in temperature range 320K to 390K. The change in the Seebeck coefficient of the FGM showed a 70% increase from the single material specimens. This boost indicated a reduction in carrier density across the interface, theorized to be influenced by the interface of the FGM.

Furthermore, to better explore the findings, the samples were compared with a standard constantan calibration sample (Figure 32) made of 55% copper and 45% nickel (Figure 30, Figure 31). At 320K, the FGM showcased a similar electrical resistivity with the constantan but at 390K, approximately 40% higher. In other words, the FGM displayed comparable electrical conductivity with the constantan at 320K. However, at 390K, it displayed a ~72% reduction in conductivity in comparison with the constantan. More importantly, the constantan presented n-type semiconductor behaviors while the FGM exhibited those of the p-type. The finding indicated that the FGM preserve its original materials' p-type behaviors.
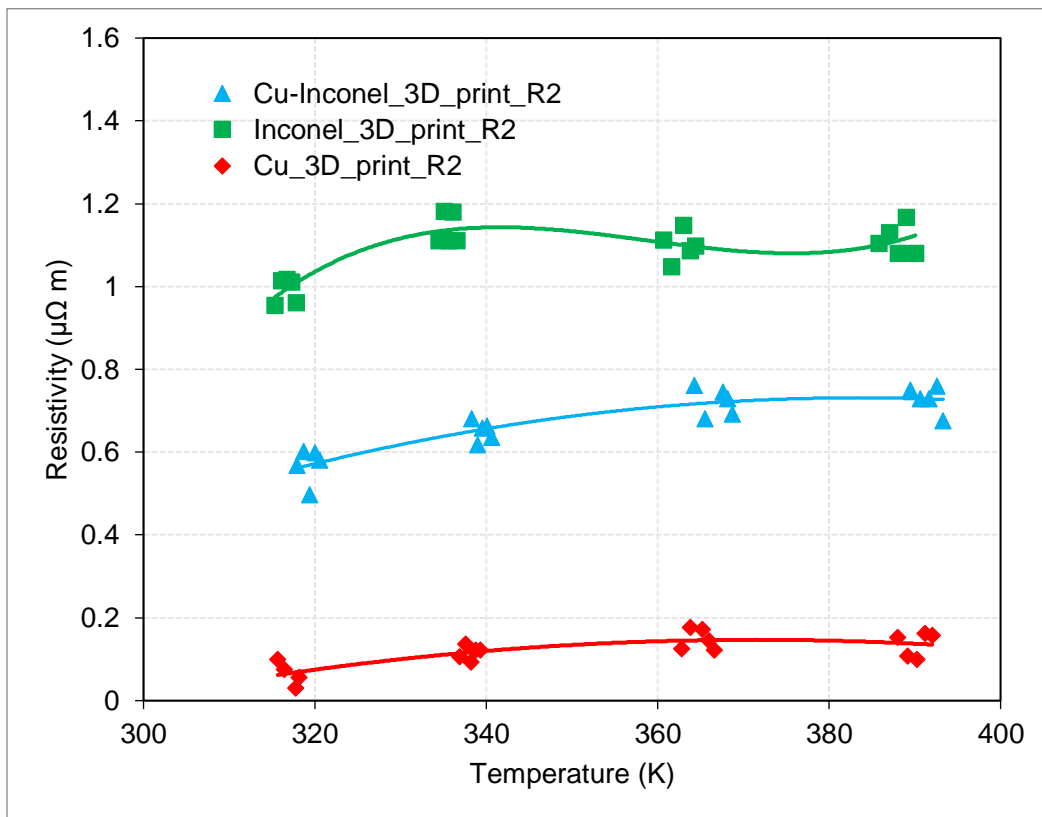
Figure 28. Electrical resistivity of the three samples
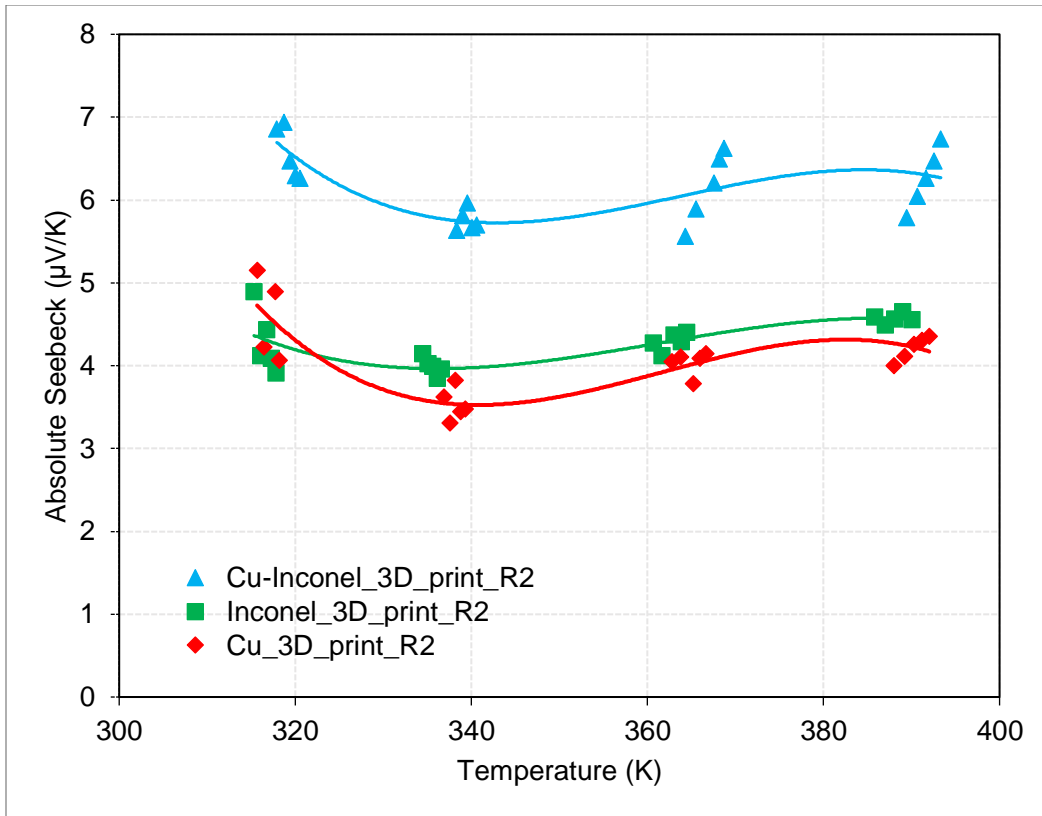
Figure 29. Absolute Seebeck coefficient of the three samples
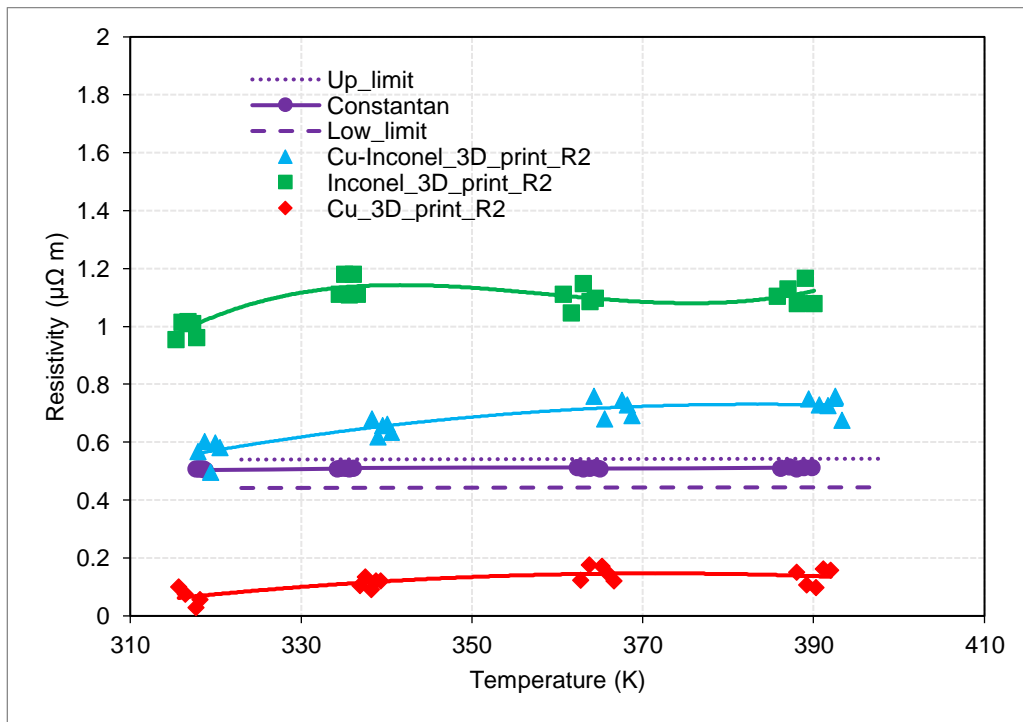
Figure 30. Electrical resistivity of the three samples vs. Cu-Ni constantan
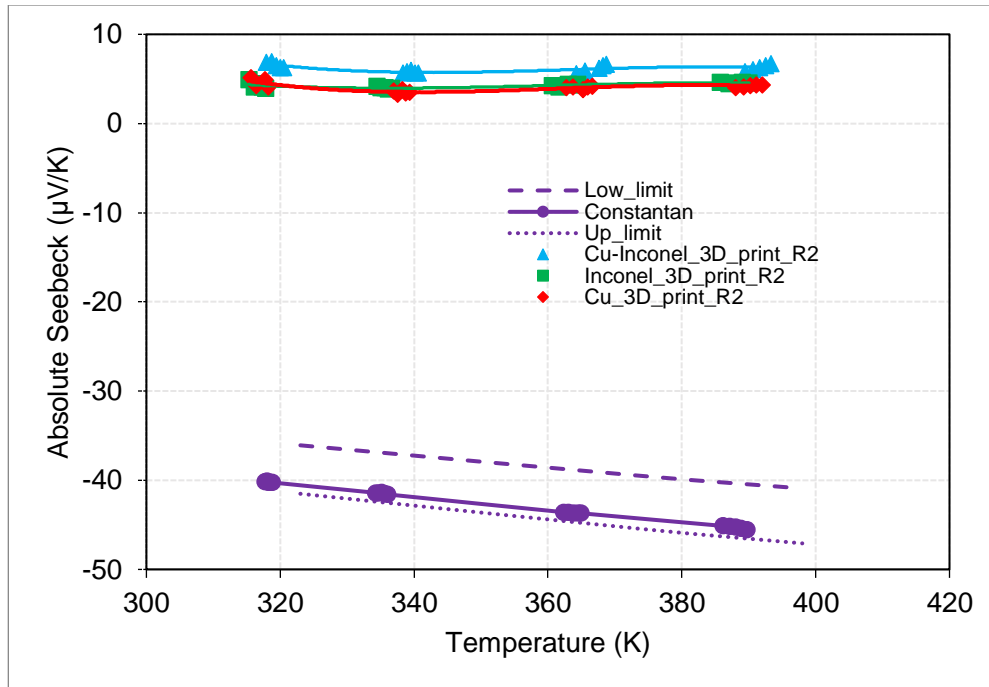
Figure 31. Absolute Seebeck of the three samples vs. Cu-Ni constantan

Figure 32. Constantan calibration sample (55%Cu, 45%Ni)

4.4. Compressive Strength Test

Figure 33 demonstrates the stress-strain curve obtained from the compressive strength test. The maximum compressive stress derived from Figure 33 was approximately 500MPa. The deformation happened mainly in the CuSn10 zone and appeared to be a 'folding' deformation. Other than the indulged effect of deformation in CuSn10 region, the rest of the specimen did not show deformation (Figure 34). There were no buckling nor deformation at or around the interface of the FGM, showing presence of metallurgical bonding between the regions, further verifying previous findings.
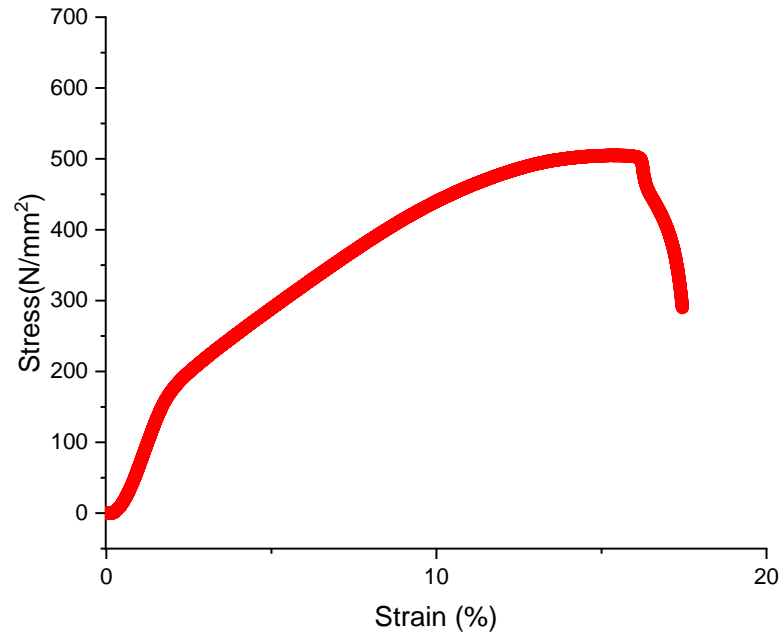
Figure 33. Stress-strain curve of the FGM
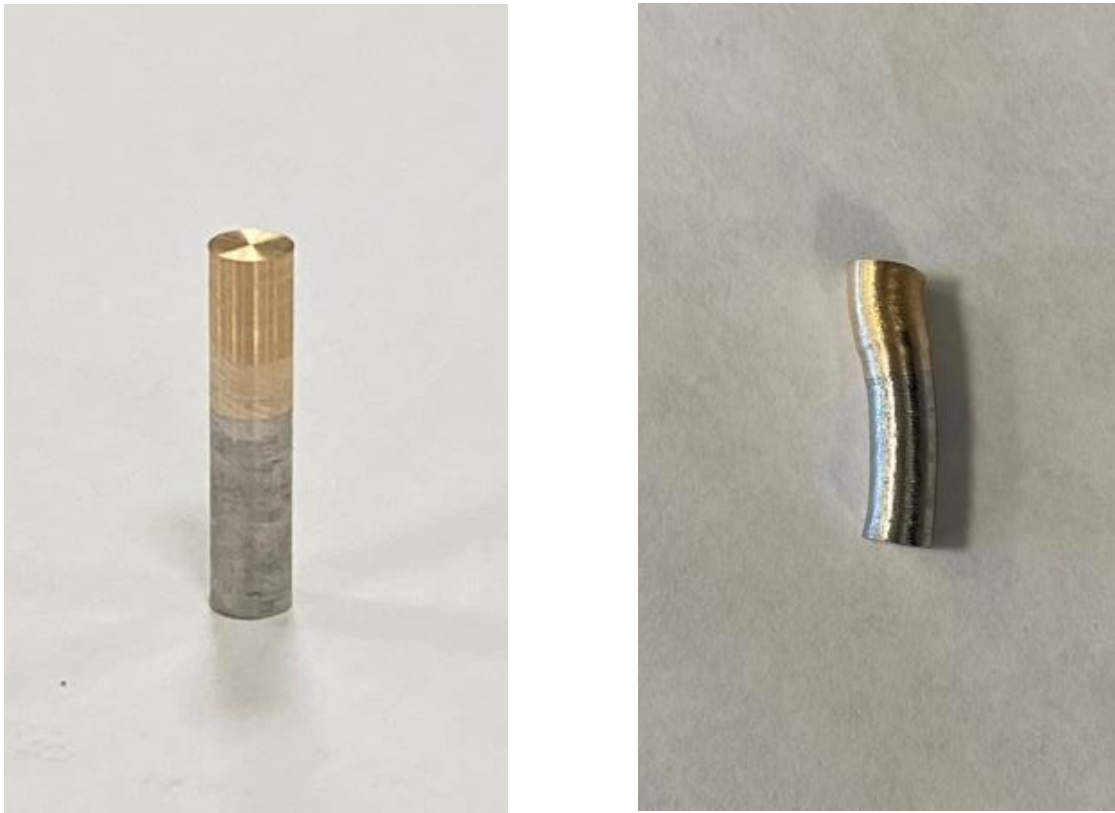
Figure 34. Compressive strength test specimen before (left) and after(right)

5. Conclusions & Future Research Recommendations

The fabrication of CuSn10-Inconel 718 FGMs via DED using the AMBIT Hybrid system was successfully conducted. The optimized parameter for the obtained CuSn10 powder was identified and applied to the sample production though only through visual criterium and trial-and-error method due to the time limitation. For future works, it is suggested that a full factorial experimental design coupled with statistical hypothesis testing be carried out to improve the optimization process and henceforth the quality of the printed samples.

The specimens showcased evident metallurgical bonding at the interface. A defined interface as well as CuSn10 and Inconel 718 regions were distinguished via microscopic imaging and SEM. On the contrary, while apparently present, the interface between CuSn10 and Inconel 718 was not smooth. Surface diffusion and penetration of one type of material into the other region was influenced by the high compatibility between copper and nickel, which created a complex and properties-variable interface.

Porosity was observed in both regions of the materials and a potential crack in the surface of the Inconel 718 region might enhance the diffusion effect. A possible secondary phase might form as an effect of the material diffusion. EDS further validated the findings via microscopic imaging and SEM and additionally indicated enriched Mo, Nb, and Cr particles potentially formed a secondary phase with CuSn10. Additional microstructure analysis such as transmission electron microscopy (TEM) is required in the future to provide a better understanding of the secondary phase.

The hardness profile across the interface of the FGM showcased increase when depart from CuSn10 region towards the interface and the Inconel 718 region. The transition of hardness was sharp and relatively abrupt. High variation in hardness at the interface of the FGM induced by the effect of material diffusion and powder penetration due to the high compatibility of copper and nickel. Though presented high variability, the interface of the FGM exhibited significantly higher hardness when compared to CuSn10 region, showcasing the improved characteristic thanks to the presence of Inconel 718.

Similarly, the conductivity and Seebeck coefficient measurements were induced by the interface of the FGM. CuSn10 indicated the highest electrical conductivity across the surface of the FGM while Inconel 718 the lowest. More importantly, the electrical conductivity at the interface of the FGM was significantly enhanced in comparison to the Inconel 718 sample. Likewise, the finding indicated that the presence of CuSn10 enhanced the electrical conductivity of the FGM, further validating the inheritance effect of FGM.

In addition, the absolute Seebeck coefficient of the FGM also reflected a 70% increase from the single-material region. The increase in Seebeck coefficient could be associated with the reduction in surface carrier density. This booster in absolute Seebeck coefficient was theorized to be influenced by the interface of the FGM. Furthermore, it was found that the FGM preserves its original materials' p-type semiconductor behaviors, instead of exhibiting n-type. In the future, it is recommended that FGMs with more than two regions of materials be studied to further explore the effects of interfaces on electrical conductivity and Seebeck coefficient changes. New materials can also be introduced in place of CuSn10 or Inconel 718 to investigate the same effects.

Last but not least, manufacturing FGMs with stepwise gradient was often associated with interfacial defects such as cracks and delamination. While showcasing superiority to conventional methods, it seems that AM faced the same problems when joining dissimilar materials, despite the high compatibility. Compositional gradient FGMs were discussed as a means to overcome such negative performances (Carroll et al., 2016; Yang et al., 2022). In future studies, more than one specimen with different gradient type shall be fabricated to investigate this claim.

References

Articek, U., Milfelner, M., & Anzel, I. (2013). Synthesis of functionally graded material H13/Cu by LENS technology. *Advances in Production Engineering & Management*, *8*(3), 169–176. https://doi.org/10.14743/apem2013.3.164

Carroll, B. E., Otis, R. A., Borgonia, J. P., Suh, J., Dillon, R. P., Shapiro, A. A., Hofmann, D. C., Liu, Z.-K., & Beese, A. M. (2016). Functionally graded material of 304L stainless steel and inconel 625 fabricated by directed energy deposition: Characterization and thermodynamic modeling. *Acta Materialla*, *108*, 46–54. https://doi.org/10.1016/j.actamat.2016.02.019

Chaudhary, V., Sai Kiran Kumar Yadav, N. M., Mantri, S. A., Dasari, S., Jagetia, A., Ramanujan, R. v., & Banerjee, R. (2020). Additive manufacturing of functionally graded Co–Fe and Ni–Fe magnetic materials. *Journal of Alloys and Compounds*, *823*. https://doi.org/10.1016/j.jallcom.2020.153817

Chen, Y., & Liou, F. W. (2018). *Additive Manufacturing of Metal Functionally Graded Materials: A Review*. https://scholarsmine.mst.edu/mec_aereng_facwork

Dubinin, O. N., Chernodubov, D. A., Kuzminova, Y. O., Shaysultanov, D. G., Akhatov, I. S., Stepanov, N. D., & Evlashin, S. A. (2021). *Gradient soft magnetic materials produced by additive manufacturing from non-magnetic powders*.

Era, Israt Zarin. (2021). Prediction of Tensile Behaviors of L-DED 316 Stainless Steel parts using Machine Learning. *Graduate Theses, Dissertations, and Problem Reports*. 8274. https://researchrepository.wvu.edu/etd/8274

Ghanavati, R., Naffakh-Moosavy, H., & Moradi, M. (2021). Additive manufacturing of thin-walled SS316L-IN718 functionally graded materials by direct laser metal deposition. *Journal of Materials Research and Technology*, *15*, 2673–2685. https://doi.org/10.1016/j.jmrt.2021.09.061

Gibson, I., Rosen, D., & Stucker, B. (2014). *Additive Manufacturing Technologies 3D Printing, Rapid Prototyping, and Direct Digital Manufacturing* (2nd ed.). Springer.

Ji, S., Sun, Z., Zhang, W., Chen, X., Xie, G., & Chang, H. (2020). Microstructural evolution and high temperature resistance of functionally graded material Ti-6Al-4V/Inconel 718 coated by directed energy deposition-laser. *Journal of Alloys and Compounds*, *848*. https://doi.org/10.1016/j.jallcom.2020.156255

Karnati, S., Sparks, T. E., Liou, F., Newkirk, J. W., Taminger, K. M. B., & Seufzer, W. J. (2015). *LASER METAL DEPOSITION OF FUNCTIONALLY GRADIENT MATERIALS FROM ELEMENTAL COPPER AND NICKEL POWDERS*.

Kim, S. H., Lee, H., Yeon, S. M., Aranas, C., Choi, K., Yoon, J., Yang, S. W., & Lee, H. (2021). Selective compositional range exclusion via directed energy deposition to produce a defect-free Inconel 718/SS 316L functionally graded material. *Additive Manufacturing*, *47*. https://doi.org/10.1016/j.addma.2021.102288

Koizumi, M. (1997). FGM activities in Japan. In *Composites Part B* (Vol. 28).

Lin, L., Syed, W. U. H., & Pinkerton, A. J. (2006). Rapid additive manufacturing of functionally graded structures using simultaneous wire and powder laser deposition. *Virtual and Physical Prototyping*, *1*(4), 217–225. https://doi.org/10.1080/17452750601141523

Makarenko, K., Dubinin, O., & Shishkovsky, I. (2020). Analytical Evaluation of the Dendritic Structure Parameters and Crystallization Rate of Laser-Deposited Cu-Fe Functionally Graded Materials. *Materials*, *13*. https://doi.org/10.3390/ma13245665

Makarenko, K. I., & Shishkovsky, I. v. (2020). Direct Energy Deposition of Cu-Fe System Functionally Graded Structures. *IOP Conference Series: Materials Science and Engineering*, *969*(1). https://doi.org/10.1088/1757-899X/969/1/012104

Meng, W., Zhang, W., Zhang, W., Yin, X., & Cui, B. (2020). Fabrication of steel-Inconel functionally graded materials by laser melting deposition integrating with laser synchronous preheating. *Optics and Laser Technology*, *131*. https://doi.org/10.1016/j.optlastec.2020.106451

Mikler, C. v., Chaudhary, V., Borkar, T., Soni, V., Jaeger, D., Chen, X., Contieri, R., Ramanujan, R. v., & Banerjee, R. (2017). Laser Additive Manufacturing of Magnetic Materials. *JOM*, *69*(3), 532–543. https://doi.org/10.1007/s11837-017-2257-2

Molitch-Hou, M. (2018). 1 - Overview of additive manufacturing process. In J. Zhang & Y.-G. Jung (Eds.), *Additive Manufacturing* (pp. 1–38). Butterworth-Heinemann. https://doi.org/https://doi.org/10.1016/B978-0-12-812155-9.00001-3

Nickel Institute. (n.d.). *Applications of copper-nickel alloys*.

Onuike, B., & Bandyopadhyay, A. (2019). Bond Strength Measurement for Additively Manufactured Inconel 718- GRCop84 Copper Alloy Bimetallic Joints. *Addit Manuf*, *27*, 576–585. https://doi.org/10.1016/j.addma.2019.04.003

Onuike, B., Heer, B., Bandyopadhyay, A., & Keck, W. M. (2018). *Additive Manufacturing of Inconel 718-Copper Alloy Bimetallic Structure using Laser Engineered Net Shaping (LENS TM)*. http://www.elsevier.com/open-access/userlicense/1.0/

Ostolaza, M., Arrizubieta, J. I., Lamikiz, A., & Cortina, M. (2021). Functionally graded AISI 316L and AISI H13 manufactured by L-DED for die and mould applications. *Applied Sciences (Switzerland)*, *11*(2), 1–11. https://doi.org/10.3390/app11020771

Shen, C., Pan, Z., Cuiuri, D., Roberts, J., & Li, H. (2016). Fabrication of Fe-FeAl Functionally Graded Material Using the Wire-Arc Additive Manufacturing Process. *Metallurgical and Materials Transactions B: Process Metallurgy and Materials Processing Science*, *47*(1), 763–772. https://doi.org/10.1007/s11663-015-0509-5

Shishkovsky, I., Kakovkina, N., & Missemer, F. (2016). Three-dimensional (3-D) laser cladding of functionally graded structures in Ni-Cr-Al system Three-Dimensional (3-D) Laser Cladding of Functionally Graded Structures in the Ni-Cr-Al System. *Lasers in Eng*, *0*, 1–15. https://faculty.skoltech.ru/people/igorshishkovsky

Singh, R., Bhavar, V., Kattire, P., Thakare, S., Patil, S., & Singh, R. K. P. (2017). A Review on Functionally Gradient Materials (FGMs) and Their Applications. *IOP Conference Series: Materials Science and Engineering*, *229*(1). https://doi.org/10.1088/1757-899X/229/1/012021

Sun, Z., Chueh, Y. H., & Li, L. (2020). Multiphase mesoscopic simulation of multiple and functionally gradient materials laser powder bed fusion additive manufacturing processes. *Additive Manufacturing*, *35*. https://doi.org/10.1016/j.addma.2020.101448

Yadav, S., Jinoop, & A. N., Sinha, N., Paul, C. P., & Bindra, K. S. (2020). Parametric investigation and characterization of laser directed energy deposited copper-nickel graded layers. *The International Journal of Advanced Manufacturing Technology* , *108*, 3779–3791. https://doi.org/10.1007/s00170-020-05644-9/Published

Yan, L., Chen, Y., & Liou, F. (2019). *Invited Review Article: Additive Manufacturing of Functionally Graded Metallic Materials Using Laser Metal Deposition*. https://www.sciencedirect.com/science/article/pii/S2214860418308364

Yang, S. W., Yoon, J., Lee, H., & Shim, D. S. (2022). Defect of functionally graded material of inconel 718 and STS 316L fabricated by directed energy deposition and its effect on

mechanical properties. *Journal of Materials Research and Technology*, *17*, 478–497. https://doi.org/10.1016/j.jmrt.2022.01.029

Yao, J., Xin, B., Gong, Y., & Cheng, G. (2021). Effect of initial temperature on the microstructure and properties of stellite-6/inconel 718 functional gradient materials formed by laser metal deposition. *Materials*, *14*(13). https://doi.org/10.3390/ma14133609

Yarrapareddy, E., Zekovic, S., Hamid, S., & Kovacedvic, R. (2006). The development of nickel–tungsten carbide functionally graded materials by a laser-based direct metal deposition process for industrial slurry erosion applications. *Proc. IMechE Part B: J. Engineering Manufacture1923*, *220*, 1923–1936. https://doi.org/10.1243/09544054JEM578

Yin, S., Yan, X., Chen, C., Jenkins, R., Liu, M., & Lupoi, R. (2018). Hybrid additive manufacturing of Al-Ti6Al4V functionally graded materials with selective laser melting and cold spraying. *Journal of Materials Processing Technology*, *255*, 650–655. https://doi.org/10.1016/j.jmatprotec.2018.01.015

Zhang, X., Li, L., & Liou, F. (2021). Additive manufacturing of stainless steel – Copper functionally graded materials via Inconel 718 interlayer. *Journal of Materials Research and Technology*, *15*, 2045–2058. https://doi.org/10.1016/j.jmrt.2021.09.027

Zhang, X., & Liou, F. (2019). Fabrication of SS316L-IN625 functionally graded materials by powder-fed directed energy deposition. *Science and Technology of Welding and Joining*, *24*(5), 504–516. https://doi.org/10.1080/13621718.2019.1589086

Appendix 1 – Mapping for Hardness

Original mapping of the specimen (Pre data-cleaning)

				Zone			
			< IN718	Interface	CUSN10 >		
(mm)	-3	-2	-1	0	1	2	3
2				9			
1.5	51	44	37	8	16	23	30
1	50	43	36	7	15	22	29
0.5	49	42	35	6	14	21	28
0	45	38	31	1	10	17	24
-0.5	46	39	32	2	11	18	25
-1	47	40	33	3	12	19	26
-1.5	48	41	34	4	13	20	27
-2				5			

Final mapping (Post data-cleaning)

				Zone			
			< IN718	Interface	CUSN10 >		
(mm)	-3	-2	-1	0	1	2	3
2				◆			
1.5	◆	◆	◆	◆	◆	◆	
1	◆	◆	◆	◆	◆	◆	
0.5	◆	◆	◆	◆	◆	◆	
0	◆	◆	◆	◆	◆	◆	
-0.5	◆	◆	◆	◆	◆	◆	
-1	◆	◆	◆	◆	◆	◆	
-1.5	◆	◆	◆	◆	◆	◆	
-2				◆			

Appendix 2 – Mapping and Results for Hardness Test 2

		Zone	
	Inconel 718	Interface	CuSn10
(mm)	-1.5		1.5
3	◆	◆	◆
2.5	◆	◆	◆
2	◆	◆	◆
1.5	◆	◆	◆
1	◆	◆	◆
0.5	◆	◆	◆
0	◆	◆	◆
-0.5		◆	

Data point	Hardness CuSn10	Data point	Hardness Interface	Data point	Hardness Inconel 718
1	138.7	8	278.7	16	279.8
2	136.3	9	179.8	17	268.0
3	145.8	10	298.1	18	286.3
4	135.5	11	190.4	19	283.9
5	139.5	12	236.8	20	274.1
6	135.5	13	207.0	21	275.8
7	141.8	14	262.7	22	276.4